Solution Structure and Dynamics of the Plasminogen Kringle 2−AMCHA Complex: 3_1-Helix in Homologous Domains[†,‡]

Daniel N. Marti,[§] Johann Schaller,[||] and Miguel Llinás*[,§]

Department of Chemistry, Carnegie Mellon University, Pittsburgh, Pennsylvania 15213, and Department of Chemistry and Biochemistry, University of Bern, CH-3012 Bern, Switzerland

Received July 27, 1999; Revised Manuscript Received September 27, 1999

ABSTRACT: The kringle 2 (K2) module of human plasminogen (Pgn) binds L-lysine and analogous zwitterionic compounds, such as the antifibrinolytic agent *trans*-(aminomethyl)cyclohexanecarboxylic acid (AMCHA). Far-UV CD and NMR spectra reveal little conformational change in K2 upon ligand binding. However, retarded $^1H-^2H$ isotope exchange kinetics induced by AMCHA indicate stabilization of the K2 conformation by the ligand. Assessment of secondary structure content from CD spectra yields ∼26% β-strand, ∼13% β-turn, ∼15% 3_1-helix, and ∼6% 3_{10}-helix. The NMR solution conformation of the K2 domain complexed to AMCHA has been determined [heavy atom rmsd = 0.49 ± 0.09 Å (backbone) and 1.02 ± 0.08 Å (all)]. The K2 molecule has overall dimensions of ∼34.5 Å × ∼33.4 Å × ∼22.7 Å. Analogous with the polypeptide outline of homologous domains, K2 contains three short antiparallel β-sheets (paired strands 15−16/20−21, 24−25/48−49, and 62−64/72−74) and four defined β-turns (residues 6−9, 16−19, 53−56, and 67−70). Consistent with the CD analysis, albeit novel in the context of kringle folding, the NMR structure reveals an unpaired β-strand structured by residues 30−32, a turn of 3_{10}-helix comprising residues 38−41, and a 3_1-helix for residues 21−24 and 74−79. We also identify alignable 3_1-helices in previously reported homologous kringle structures. Rather high order parameter S^2 values ($\langle S^2\rangle \sim 0.85 \pm 0.04$) characterize the K2 backbone dynamics. The lowest flexibility is observed for the two inner loop segments of residues 51−63 and 63−75 ($\langle S^2\rangle \sim 0.86-0.87 \pm 0.03$). Overhauser connectivities reveal close hydrophobic contacts of the ligand ring with side chains of Tyr^{36}, Trp^{62}, Phe^{64}, Trp^{72}, and Leu^{74}. In most K2 structures, the N atom of AMCHA places itself ∼3.9 and ∼4.4 Å from the anionic groups of Glu^{57} and Asp^{55}, respectively, while its carboxylate group, H-bonded to the Tyr^{36} side chain OH^{η}, ion-pairs the Arg^{71} guanidinium group. Consistent with the preference of K2 for binding 5-aminopentanoic acid over 6-aminohexanoic acid, the positions of the ionic centers within the K2 binding site approach each other ∼1 Å closer relative to what is observed in lysine binding sites of homologous Pgn modules.

Plasmin (Plm)[1] and its proenzyme, plasminogen (Pgn), interact noncovalently with a variety of proteins, including the substrates fibrin and fibrinogen (*1*), the inhibitor α_2-antiplasmin (*2*), the histidine-rich glycoprotein (*3*), and thrombospondin-1 (*4*). These interactions are mediated via lysine binding sites (LBS) in the kringle modules of Pgn. In addition, complexation of lysyl-type ligands relaxes the compact conformation of the Pgn molecule (reviewed in ref *5*). Therefore, kringles play crucial roles both in substrate recognition by and in determining the conformation of Pgn, thus regulating its susceptibility to proteinase activators. In addition, Pgn binding sites have been identified on surfaces of a number of cells such as platelets and endothelial cells (*6*, *7*). In this context, the isolated modules kringle 1 (K1), K2, K3, K4, and K5 variously exhibit inhibitor activity, similar to that of Angiostatin, against basic fibroblast growth factor-induced endothelial cell proliferation (*8*, *9*) and cell migration (*10*, *11*).

The kringle modules of Pgn comprise ∼80 amino acid residues, and their folding is constrained by Cys residues pairwise connected in a characteristic 1−80, 22−63, 51−

[†] This research was supported by U.S. Public Health Service Grant HL-29409 (NIH).

[‡] The coordinates have been deposited in the Brookhaven Protein Databank (file name 1B2I).

* To whom correspondence should be addressed. E-mail: llinas+@andrew.cmu.edu. Telephone: (412) 268-3140. Fax: (412) 268-1061.

[§] Carnegie Mellon University.

[||] University of Bern.

[1] Abbreviations: 5-APA, 5-aminopentanoic acid; 6-AHA, 6-aminohexanoic acid; AMCHA, *trans*-(aminomethyl)cyclohexanecarboxylic acid; CD, circular dichroism; CDIH, dihedral angle restraint; COSY, two-dimensional chemical shift correlated spectroscopy; EM, energy minimization; HSQC, heteronuclear single-quantum coherence; K1, kringle 1 domain of Pgn ($Cys^{84}-Cys^{162}$); K2, kringle 2 domain of Pgn ($Cys^{166}-Cys^{243}$), generated as r-K2; K3, kringle 3 domain of Pgn ($Cys^{256}-Cys^{333}$); K4, kringle 4 domain of Pgn ($Cys^{358}-Cys^{435}$); K5, kringle 5 domain of Pgn ($Cys^{462}-Cys^{541}$); K_a, equilibrium association constant; LBS, lysine binding site; MD, molecular dynamics; NOE, nuclear Overhauser effect; NOESY, two-dimensional NOE-correlated spectroscopy; Pgn, human plasminogen; pH*, glass electrode pH reading, uncorrected for the deuterium isotope effect; Plm, human plasmin; r-K2, recombinant Pgn fragment C162T/E163S/EE[K2/C169G]T containing mutations C162T, E163S, and C169G; TOCSY, two-dimensional total correlation spectroscopy; rmsd, root-mean-square deviation; sc, side chain; τ_c, effective isotropic rotational correlation time; τ_{mix}, mixing time; T_1, longitudinal spin−lattice relaxation time; T_2, transverse spin−spin relaxation time; tPA, human tissue-type plasminogen activator; TPPI, time-proportional phase increment; TSP, sodium 3-(trimethylsilyl)[2,2,3,3-$^2H_4$]propionate; uPA, human urokinase-type plasminogen activator; vdW, van der Waals; wt, wild-type.

10.1021/bi9917378 CCC: $18.00
Published on Web 11/11/1999

75 disulfide bond pattern.[2] Structure elucidation of ligand-complexed kringle modules (*14*−*18*) as well as ligand-binding experiments with wild-type (wt) (*19*−*22*) and site-specific mutated domains (*23*−*25*) have led to the localization of amino acid residues relevant for the interaction with dipolar, lysyl-type ligands. In particular, it is now well established that in K1, K2, K4, and K5 the ligand's amino group ion-pairs acidic residues at positions 55 and 57 while its carboxylate group variously interacts with Arg^{71} (K1 and K4), Arg^{35} (K1), or Lys^{35} (K4). In K3, a Lys residue occupies position 57; as a consequence, K3 does not interact with lysine-type zwitterions (*26*, *27*). Furthermore, the ligand hydrocarbon moiety establishes van der Waals contact with aromatic residues Phe^{36} (K1 and K5), Trp^{62}, Tyr^{64}/Phe^{64}, and Tyr^{72}/Trp^{72} (K1, K4, and K5), thus stabilizing the interaction.

All the homologous lysine-binding kringles bind the Pgn N-terminal loop segment, implying potential role(s) in determining the macrostructure of Glu^1−Pgn (*28*, *29*). However, with regard to their selectivity for linear ω-aminocarboxylic acids, K1, K4, and K5 exhibit the strongest affinity for 6-aminohexanoic acid (6-AHA), while K2 shows a preference for 5-aminopentanoic acid (5-APA), an analogue with a shorter hydrocarbon chain (*30*). This suggests a structurally different array of residues at the K2 LBS.

The Pgn K2 and K3 domains stand out among homologous motifs found in kringle-containing proteins in that they are cross-linked via a disulfide bond which involves Cys residues at positions 4 (K2) and 43 (K3). This generates a K2+3 "supermodule" (*27*) in which one kringle has the ability to bind lysine (K2) while the other does not (K3), hinting at a unique, as yet uncharacterized, functionality for the coupled pair. In this paper, the solution conformation of the Pgn K2 complexed to the antifibrinolytic drug *trans*-(aminomethyl)-cyclohexanecarboxylic acid (AMCHA) is described, novel NMR evidence for a direct involvement of the Glu^{57} and Arg^{71} side chains in ligand complexation is presented, the occurrence of 3_1-helix is reported, and the K2 backbone dynamics are discussed. Our study represents a first step toward a functional−structural characterization of the K2+3 supermodule and of interactions between the two domains.

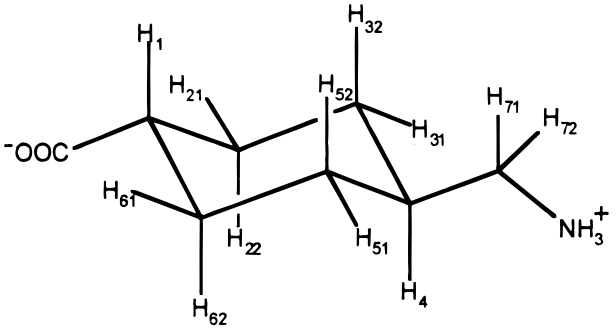

AMCHA

EXPERIMENTAL PROCEDURES

Generation of Recombinant K2 (r-K2). Cloning of the Pgn K2 cDNA and its expression in *Escherichia coli*, as well as the protein refolding and purification protocols, have been reported elsewhere (*26*, *30*). ^{15}N labeling of the domain was achieved in M9 medium (pH 7.4) supplemented with 5 mg of $FeCl_3 \cdot 6H_2O$, 1 mg of thiamine, and 10 g of glucose per liter (*31*). For ^{13}C labeling, 2 g of [$^{13}C_6$]-D-glucose (99 at. % ^{13}C, Isotec Inc., Miamisburg, OH) was employed per liter. The purity and correct folding of the isolated r-K2 were verified by SDS−PAGE and ^1H NMR spectroscopy, respectively.

CD Analysis of K2. Circular dichroism (CD) spectra were acquired at 37 °C on a Jasco J-715 spectropolarimeter using a 0.5 cm cell. r-K2 was dissolved at a concentration of 2.25 μM and the pH adjusted to 5.13. Spectra were recorded in the 178−260 nm wavelength range and averaged over five scans at a speed of 20 nm/min and 0.5 nm resolution. Spectra in the presence of AMCHA were recorded with a 200-fold molar excess of ligand. K2 secondary structure content was assessed with the program CDsstr version 1.8 (*32*).

NMR Sample Preparation. Unlabeled or ^{15}N-enriched r-K2 was dissolved in 300 μL of 90% ^1H_2O/10% ^2H_2O (99.996 at. % ^2H, Isotec Inc.) at a concentration of ~3.2 mM. In the case of the ^{13}C-labeled protein, the concentration was ~1.2 mM. The pH* was adjusted to 5.12 by addition of ^2HOAc or NaO^2H. To study the AMCHA-complexed K2, ligand was added to protein samples to achieve a 1:3 r-K2:AMCHA molar concentration ratio.

NMR Spectroscopy and Data Processing. Data from all NMR experiments were recorded in quadrature, at 37 °C, on Bruker Avance DRX spectrometers equipped with triple-resonance z-gradient probes. Homonuclear two-dimensional spectra were acquired at 600 MHz using TPPI. For COSY (*33*) and double-quantum-filtered COSY (*34*) experiments, water suppression was achieved by selective low-power irradiation during the 0.8 s relaxation delay between scans. Data from TOCSY experiments were recorded with MLEV17, isotropic mixing times (τ_{mix}) of 35 and 75 ms (*35*). Data from NOESY experiments (*36*) were collected with six τ_{mix} values, set within the range of 60−350 ms. For both NOESY and TOCSY, the 3-9-19 pulse sequence with gradients was used for water suppression (*37*). Data were processed with FELIX version 95 (Molecular Simulations Inc., San Diego, CA). Time domain data in t_1 were zero-filled to 4K data points; resolution enhancement was accomplished via straight (COSY) or 45°-shifted squared (TOCSY and NOESY) sine-bell window functions along both dimensions.

^{15}N-edited NMR spectra were acquired at 500 MHz. A sensitivity-enhanced version of the two-dimensional ^1H−^{15}N HSQC experiment (*38*) was carried out according to ref *39*. Water suppression was achieved with gradients via the 3-9-19 pulse sequence. Linear prediction to 256 complex points was implemented along t_1; 45°-shifted squared sine-bell window functions were applied along both t_1 and t_2. ^{15}N-edited NOESY-HSQC spectra (*40*, *41*) were acquired with τ_{mix} of 75 and 150 ms and ^{15}N-edited TOCSY-HSQC spectra (*42*) with MLEV17, τ_{mix}s of 35 and 75 ms. Data were collected in the phase-sensitive mode using TPPI for t_1 (^1H) and echo/antiecho-TPPI gradient selection (*43*) for t_2 (^{15}N). ^{15}N-edited HNHA (*44*) and HNHB spectra (*45*,*46*) were acquired in the States phase-sensitive mode along both t_1 (^1H) and t_2 (^{15}N).

^{13}C- and ^{15}N-edited spectra were recorded at 600 MHz. Quadrature in t_1 (^1H and ^{13}C) and t_2 (^{15}N) of the HNCA (*47*, *48*), HN(CO)CA (*49*), and HCC(CO)NH (*50*−*52*) experi-

[2] We adhere to the standard kringle amino acid residue numbering convention (*12*, *13*).

ments was achieved via the States−TPPI and echo/antiecho-TPPI gradient selection mode, respectively. Data from the latter experiment were recorded with τ_{mix} of 12 and 20 ms via the DIPSI-2 scheme (*53*) for ^{13}C isotropic mixing. The WALTZ-16 scheme (*54*) was used in all experiments for ^{15}N decoupling during acquisition. Three-dimensional data were linearly predicted to 128 (t_1) and 64 (t_2) complex points, respectively, and 45°- or 60°-shifted (HNHA, HNHB) squared sine-bell functions were applied along all three dimensions. The matrix size for three-dimensional spectra was 512 × 512 × 128. ^1H chemical shifts are referred to the TSP resonance using *p*-dioxane as the internal standard (*55*). ^{13}C and ^{15}N chemical shifts also are relative to TSP (*56*).

Hydrogen Exchange Experiments. $^1H-^2H$ exchange kinetics of backbone amide protons was monitored by recording a series of $^1H-^{15}N$ HSQC spectra at 22 °C at various times after dissolving the sample in ^2H_2O, pH* 5.12. Intervals between spectra were initially 40 min (10 spectra) and were extended to 165 min (last 10 spectra). Additional data were acquired after 7 and 14 days.

Torsion Angle Restraints and Stereospecific Assignment. Values for H^N-H^α spin−spin coupling constants ($^3J_{HN\alpha}$) were obtained from the HNHA experiment via analysis of diagonal to cross-peak intensity ratios (*44*). To $^3J_{HN\alpha}$ values of ≥8 (22 residues) and ≤6 Hz (22 residues), ϕ torsion angles were assigned to lie within ranges of −160° to −80° and −90° to −30°, respectively (*57, 58*). Stereospecific assignments of H^β protons and identification of 35 χ_1 torsion angles were achieved on the basis of $^3J_{\alpha\beta}$ and $^3J_{N\beta}$ data extracted from COSY and HNHB experiments, respectively, and $H^\alpha-H^\beta$ and H^N-H^β NOE intensities obtained from a (two-dimensional) NOESY spectrum with a τ_{mix} of 120 ms.

Interproton Distance Restraints. NOE connectivities (2093) were assigned in two-dimensional NOESY experiments with the K2−AMCHA complex. Among these, 1320 unambiguously assigned intra-K2 NOESY cross-peaks were selected and interproton distances[3] estimated from the buildup of spectra recorded at τ_{mix} of 60 and 90 ms, calibrated according to fixed interproton distances. A total of 568 intraresidue, 295 sequential, 119 short-range ($1 < |i - j| < 5$), and 338 long-range ($5 \leq |i - j|$) distance restraints were thus obtained (Figure 1a). Upper and lower limits were set at ±20% of the calculated distance, respectively. An upper limit of 6 Å was set for distances derived from cross-peaks that could be observed only with long τ_{mix} (250 and 350 ms). Thirteen supplementary distance restraints were introduced to account for seven backbone CO···HN H-bonds involving residues located in β-sheet regions. Twenty-eight intermolecular K2−AMCHA distance constraints were derived from NOESY spectra recorded for K2 in the presence of 3- and 15-fold molar ligand excesses.

Structure Calculation. Structures were computed using X-PLOR 3.851 (*59*) according to a distance geometry/regularization protocol (*60, 61*). Starting from NOE data for the K2−AMCHA complex, 150 K2 substructures were generated using the X-PLOR force field "parallhdg.pro" which imposes idealized covalent geometry. Chirality and planarity were introduced during 4.5 ps of high-temperature

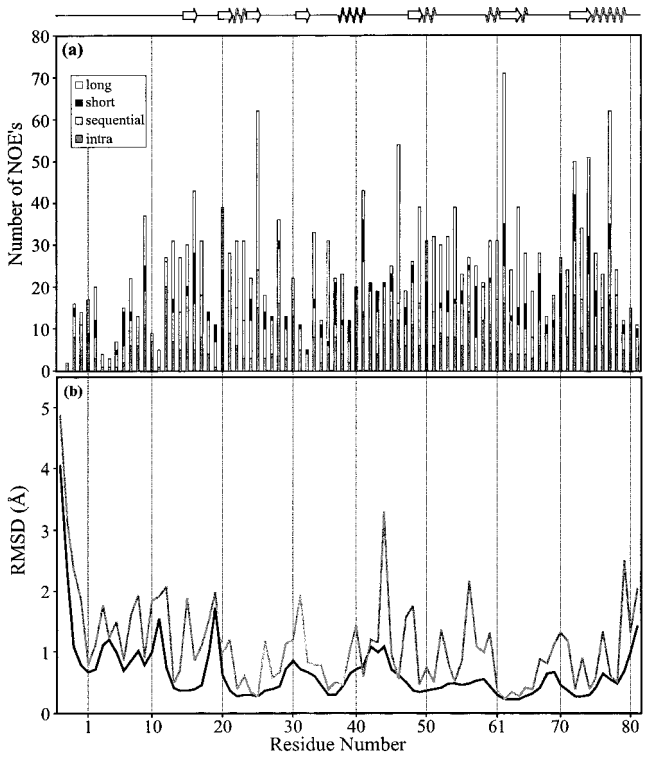

FIGURE 1: Correlation between the number of experimental distance constraints and the averaged atom rmsd from the mean for kringle 2 structures. (a) Number of NOE constraints vs K2 sequence. Intraresidue, sequential, short-range ($1 < |i - j| < 5$), and long-range ($5 \leq |i - j|$) NOEs are denoted by bars filled with four different grades of shading. (b) Sequence profile of the averaged heavy atom rmsd to the mean of backbone (N, C^α, and C′) (black) and all heavy (gray) atoms. The rmsd calculation was performed on the ensemble of 20 AMCHA-complexed K2 structures. For reference, the K2 secondary structure is outlined at the top.

(1500 K) molecular dynamics (MD) simulation. Further conformational space was sampled by simulated annealing over a period of 6 ps and stepwise temperature changes from 1500 to 100 K. The latter was followed by 200 steps of energy minimization (EM). A square-well potential was used for the NOE energy; the vdW energy was modeled by a repel function of a variable force constant. In the first round of structure refinement, NOEs accounting for disulfide bonds were introduced by setting the $S^\gamma\cdots S^\gamma$ distance between paired Cys residues to 2.02 Å. A 6 ps MD trajectory was calculated during which the temperature was lowered from 1000 to 100 K, followed by 200 steps of EM. After the S^γ atoms had been linked covalently, the refinement protocol was repeated via a 6 ps MD run that involved cooling from 600 to 100 K. Good convergence was indicated by the heavy atom rmsds for all residues within the kringle proper, namely, within the stretch of Cys^1-Cys^{80}: 0.96 ± 0.10 Å (for the backbone, 0.43 ± 0.09 Å), relative to the mean (Table 1).

The structure of the K2−AMCHA complex was computed on the basis of 28 intermolecular NOE distance constraints (Table 2), introduced after interactively docking the ligand in the vicinity of the K2 LBS within the generated kringle structures described above. MD calculations were carried out for 3 ps as described above. The force field incorporated energy terms for bonds, angles, impropers, NOEs, dihedrals, and H-bonds as well as 28 intermolecular NOEs. Electrostatic and vdW interactions were modeled by switching functions effective at a radius between 5 and 9 Å. The structures were

[3] Among these, 196 are backbone−backbone, 612 backbone−side chain, and 512 side chain−side chain.

Table 1: Statistics Profile of the Kringle 2 Structures, Including the Heavy Atom rmsd, the rmsd of Geometric Terms, and an Energy Summary

	rmsd from the mean of heavy atom coordinates[a]				
	backbone (Å)	all (Å)		backbone (Å)	all (Å)
X-PLOR (ligand-free K2)			CHARMm (K2−AMCHA complex; 2nd round of refinement)		
150 structures	0.431 ± 0.092	0.958 ± 0.099	75 structures	0.531 ± 0.111	1.045 ± 0.114
X-PLOR (K2−AMCHA complex)			CHARMm (K2−AMCHA complex; 3rd round of refinement)		
149 structures	0.443 ± 0.092	0.974 ± 0.098	20 structures	0.485 ± 0.085	1.023 ± 0.077

	rmsd of geometric terms of 20 selected structures[b]				
	NOEs (Å)	CDIH (deg)	bonds (Å)	angles (deg)	impropers (deg)
CHARMm (K2−AMCHA complex)	0.062 ± 0.005	0.659 ± 0.546	0.014 ± 0.00005	2.148 ± 0.026	3.058 ± 0.140

	averaged energies of 20 selected, final structures[c] (kcal mol^{-1}) (total energy = −993.4 ± 30.9 kcal mol^{-1})					
NOEs/CDIH	bonds	angles	impropers	dihedrals	Lennard-Jones	electrostatic
59.2 ± 5.2	21.5 ± 0.5	212.8 ± 4.2	9.6 ± 0.6	331.4 ± 7.0	−371.6 ± 6.7	−1256.4 ± 38.6

[a] By reference to the mean structure for residues Cys^{1}−Cys^{80} obtained by averaging the coordinates of the selected ensemble after best-fit superimposition of backbone atoms N, C$^{\alpha}$, and C′. [b] rmsd values for experimental NOE and CDIH refer to deviations from the upper and lower limits of the distance and dihedral angle restraints, respectively. The rmsds for bonds, angles, and impropers are calculated by reference to the idealized covalent geometry as defined in the X-PLOR "parallhdg.pro" force field. [c] Energies were calculated using the CHARMm22 force field. For the electrostatic energy, a distance-dependent dielectric constant ($\epsilon = \epsilon_0 r$, $\epsilon_0 = 1$) was used. NOE and CDIH energy terms were calculated with force constants of 30 kcal mol^{-1} Å^{-2} and 5 kcal mol^{-1} rad^{-2}.

Table 2: NOE-Derived Interproton Distances (Å) between Kringle 2 Lysine Binding Site Residues and AMCHA[a]

AMCHA	H_1	H_{22}	H_{21}	H_{62}	H_{61}	H_{32}	H_{52}	H_{51}	H_4	H_{7*}
Tyr^{36} H$^{\delta*}$		4.7								
Tyr^{36} H$^{\epsilon*}$		3.9	5.0	4.0						
Glu^{57} H$^{\beta*}$						5.0				
Trp^{62} H$^{\beta3}$				5.0						
Trp^{62} H$^{\eta2}$		4.2								
Trp^{62} H$^{\zeta2}$									3.7	
Phe^{64} H$^{\epsilon*}$				4.5	4.8					
Arg^{71} H$^{\epsilon}$					3.5					
Trp^{72} H$^{\beta3}$		4.3				4.7				
Trp^{72} H$^{\delta1}$	3.2			5.0	2.9					
Trp^{72} H$^{\epsilon1}$	3.7		5.0			4.4				
Trp^{72} H$^{\epsilon3}$		5.0			3.6					
Trp^{72} H$^{\eta2}$					4.6					3.1
Trp^{72} H$^{\zeta2}$						3.8	4.5			4.1
Trp^{72} H$^{\zeta3}$										4.9
Leu^{74} H$^{\delta2*}$								4.0		

[a] Distances calculated from the slopes of NOESY cross-peak buildups determined from NOESY spectra with τ_{mix} of 60 and 90 ms. Intraresidue Trp indole ring protons and Gly H$^{\alpha2}$−H$^{\alpha3}$ NOE buildups were used for calibration. NOESY spectra were acquired at AMCHA:K2 molar ratios of 3:1 and 15:1.

Powell energy minimized in 600 steps. Except for one, the convergence of the calculated structures was closely similar to those computed for the K2 structure when ignoring NOEs to the ligand (Table 1).

Further refinement was achieved using the CHARMm 23.2 program and CHARMm22 force field (Quanta96 software package, Molecular Simulations Inc.). After 500 steps of adopted-basis Newton−Raphson EM, a 0.96 ps MD run was implemented during which the temperature changed from 600 to ∼0 K, followed by another round of EM. Active energy terms were the same as in the X-PLOR calculation. Seventy-five structures were selected on the basis of their total energy value and Ramachandran plot, and subjected to another round of MD/EM calculations. In the subsequent, final MD/EM run, further improvement of the Ramachandran ϕ versus ψ map resulted for 20 structures selected on the basis of their total energy via a statistical analysis using programs PROCHECK-NMR version 3.4.4 (*62*), MOLMOL version 2.6 (*63*), and X-PLOR 3.851. Among these, 61.3% of the residues fell in the energetically most favored, 35.9% in the additionally allowed, 2.8% in the generously allowed, and none in the disallowed areas (*62*).

Figure 1b illustrates the average rmsd sequence profile of backbone and all heavy atoms. In the final CHARMm MD/EM run, the upper and lower limits of the distance restraints were set by adding and subtracting, respectively, 30% of the estimated distance. For the NOE distance and the experimental dihedral angle restraints, rmsds amount to 0.062 ± 0.005 Å and 0.66 ± 0.55°, respectively (Table 1). While the covalent geometry of the structures was not strictly conserved with the CHARMm22 force field, as indicated by an increased rmsd for bonds, angles, and impropers from their idealized values (Table 1), all the structures exhibit a large negative Lennard-Jones energy (average of −371.6 ± 6.7 kcal mol^{-1}), indicative of favorable nonbonded contacts.

Analysis of secondary structure was assisted by use of the program XTLsstr (*64*). All calculations were carried out on a Silicon Graphics O2 workstation equipped with a MIPS R5000 processor.

Backbone Dynamics. Dynamic behavior was assessed by measuring ^{15}N T_1 and T_2 relaxation, as well as the heteronuclear ^{1}H−^{15}N NOE (XNOE) of amide NH groups. Experiments were performed at 500 MHz as described previously (*65*). For the evaluation of T_1, nine τ delays were applied ranging from 5 to 1503 ms; for T_2, 12 τ delays between 16 and 490 ms were applied. The delay between scans was set to 1.2 and 5 s in the T_1/T_2 and XNOE experiments, respectively. The T_1 and T_2 relaxation data were fitted to exponential decay curves using FELIX version 97 (Molecular Simulations Inc.). ^{1}H−^{15}N NOEs were obtained from the peak height ratios of two ^{1}H-saturated and two unsaturated XNOE experiments. Relaxation data were analyzed on the basis of the extended model-free approach (*66*, *67*) and the Model-Free version 3.0 software (*68*). The effective isotropic rotation correlation time, τ_c, was estimated from the averaged R_2/R_1 ratio. Five models were tested against the experimental data optimizing the following free parameters: (1) generalized order parameter S^2, (2) S^2 and the internal time scale parameter τ_e, (3) S^2 and the chemical exchange parameter

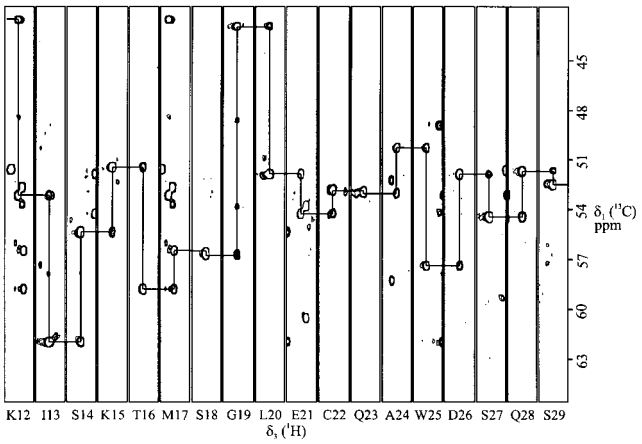

FIGURE 2: Selected expansion of the HNCA NMR spectrum of the kringle 2 segment of residues Lys[12]−Ser[29]. Strips δ_1 ($^{13}C^{\alpha}$) − δ_3 (^1H) are extracted at the δ_2 (^{15}N) and δ_3 (^1H) frequencies of the backbone NH groups of the indicated amino acids. Sequential *J*-connected C^{α} resonances are linked by lines. Spectra were recorded on a 1.2 mM r-K2 sample dissolved in 10:90 (v/v) ^2H_2O/^1H_2O at pH* 5.1 and 37 °C.

R_{ex}, (4) S^2, τ_e (fast time scale), and R_{ex}, and (5) S^2, τ_e (slow time scale), and order parameter for internal motion on fast time scale S_f^2. Values for the free parameters were initially estimated by a grid search and refined with Model-Free.

RESULTS

Kringle 2 Resonance Assignment. Sequential assignment was obtained on the basis of the two-dimensional NOESY, three-dimensional $^1H-^{15}N$ NOESY-HSQC, HN(CO)CA, and HNCA (Figure 2) experiments. Except for Pro imino and the Thr[−4], Ser[−3], and Tyr[36] amide groups, all backbone ^1H and ^{15}N resonances were assigned (Figure 3). Side chain ^1H signals were sorted via two-dimensional TOCSY, COSY, three-dimensional $^1H-^{15}N$ TOCSY-HSQC, and HCC(CO)-NH experiments. Aromatic and His imidazole spin systems had been identified previously (*30*). Resonance assignments are provided as Supporting Information.

The H^{δ} resonances of Pro residues at positions 38, 42, 54, 61, 68, and 78 yielded characteristic NOESY cross-peaks with the H^{α} resonances of their corresponding preceding residues. For Pro residues at positions 42, 54, and 61, additional $H^{\delta}-H^{N}_{(i-1)}$ NOEs were identified. Such patterns are indicative of a trans conformation for the X−Pro peptide bonds. In the case of Pro[30], an NOE between its H^{α} and the H^N of Ser[29] was detected, whereas a connectivity between Ser[29] backbone protons and the Pro[30] H^{δ} was not apparent, consistent with a cis Ser[29]−Pro[30] peptide bond.

AMCHA Binding. Among several small molecule zwitterionic ligands, AMCHA exhibits the strongest interaction with the Pgn K2 ($K_a \sim 7.2$ mM^{-1}) (*30*). HSQC spectra reveal AMCHA-induced shifts of K2 backbone and side chain $^1H-^{15}N$ resonances, with the segment Asp[55]−Leu[58] being the most sensitive to ligand binding (Figure 3). Noteworthy is the fact that Asp[55] and Glu[57] NHs display $\Delta\delta_H$ values of ∼0.34 and ∼0.26 ppm and $\Delta\delta_N$ values of ∼1.46 and ∼1.65 ppm, respectively. Neighboring residues Arg[56] and Leu[58] also exhibit significantly perturbed resonances: $\Delta\delta_H \sim 0.20$ and 0.39 ppm and $\Delta\delta_N \sim 0.77$ and 2.81 ppm, respectively. Other residues exhibiting distinct AMCHA-induced resonance shifts are Glu[7], Cys[22], Ala[32], His[33], Ile[37], and Leu[74] ($|\Delta\delta_H| > 0.13$ or $|\Delta\delta_N| > 0.4$ ppm).

As for side chains, the Trp[62] and Trp[72] aromatic $NH^{\epsilon 1}$ resonances are markedly perturbed by AMCHA: $\Delta\delta_H \sim 0.64$ and 0.23 ppm and $\Delta\delta_N \sim 0.14$ and 0.42 ppm, respectively. Most interestingly, $\Delta\delta_H \sim 1.07$ ppm and $\Delta\delta_N \sim 0.87$ ppm are observed for the Arg[71] NH^{ϵ} resonances.

Hydrogen Exchange. The kinetics of K2 $^1H-^2H$ exchange was monitored via two-dimensional $^1H-^{15}N$ HSQC experiments. In the absence of ligand, 29 NH cross-peaks remained in the spectrum 8 h after dissolving the protein in ^2H_2O (pH* 5.12 and 22 °C), including the Trp[25] $NH^{\epsilon 1}$ (Table 3). After an additional 80 h, 11 remained, five being rather weak. In the presence of AMCHA, 29 backbone amide NH cross-peaks exhibited considerable intensities after 8 h (Table 3). NH signals from Trp[25], Asn[53], and Trp[62] side chains also remained detectable. After 186 h, 22 cross-peaks were still visible in the HSQC spectrum, which was reduced to 17 within the following 144 h. The latter stemmed all from backbone amides except for the one which arises from the Trp[25] $NH^{\epsilon 1}$. The generalized retardation of the exchange kinetics induced by AMCHA indicates that the ligand stabilizes the K2 structure.

CD Analysis. Far-UV CD spectra of K2 in the absence and presence of ligand (Figure 4) reveal close conformational similarity between ligand-free and AMCHA-complexed K2. The negative ellipticity near 200 nm is evidence for irregular coil structures and distorted or short β-strands (*69*). Within the 212−236 nm range, the positive ellipticity is indicative of coil structure. Secondary structure content was estimated via the variable selection method (*32*). For the uncomplexed K2, the analysis yielded ∼23% β-strand, ∼14% β-turns, ∼14% 3_1-helix, and ∼6% 3_{10}-helix. This is comparable to ∼26% antiparallel β-strand, ∼13% β-turns, ∼15% 3_1-helix, and ∼6% 3_{10}-helix derived for the AMCHA-bound K2. No α-helix was content was indicated for either.

Kringle 2 Structure. Superposed backbone structures are illustrated in Figure 5a. The backbone heavy atom rmsd profile (Figure 1b) reveals that residues in the vicinity of Cys[22], Cys[51], and Cys[63] are the better defined ones. The latter participate in the Cys[22]−Cys[63] and Cys[51]−Cys[75] disulfide bridges, where the Cys[63] and Cys[75] S^{γ} atoms are separated by ∼3.1 Å and those from Cys[22] and Cys[51] by ∼4.7 Å. These two cystines are buried within the kringle core and juxtapose at an angle of ∼70° relative to each other, thus constraining the domain to a compact folding. The resulting structure has dimensions of ∼34.5 Å × ∼33.4 Å × ∼22.7 Å.

The domain disulfide pattern and backbone folding defines seven loops conformed by residues Cys[1]−Ile[13], Ser[14]−Cys[22], Cys[22]−Tyr[36], Ile[37]−Cys[51], Cys[51]−Cys[63], Cys[63]−Cys[75], and Cys[75]−Cys[80]. High structural resolution is obtained for the loop segments of residues Cys[22]−Tyr[36], Cys[51]−Cys[63], and Cys[63]−Cys[75], with backbone rmsds in the range of 0.31−0.35 Å. The least defined area of the molecule is the Cys[1]−Ile[13] loop, with a backbone rmsd of 0.71 ± 0.18 Å. This is consistent with the finding that the Tyr[9] aromatic protons exhibit multiple sets of NMR resonances, a reflection of a slow, local conformational exchange, as previously observed for the Pgn K1 and K4 (*16*, *70*), the tPA K2 (*14*), and the uPA kringle (*71*). Ser[14]−Cys[22], Ile[37]−Cys[51], and Cys[75]−Cys[80]

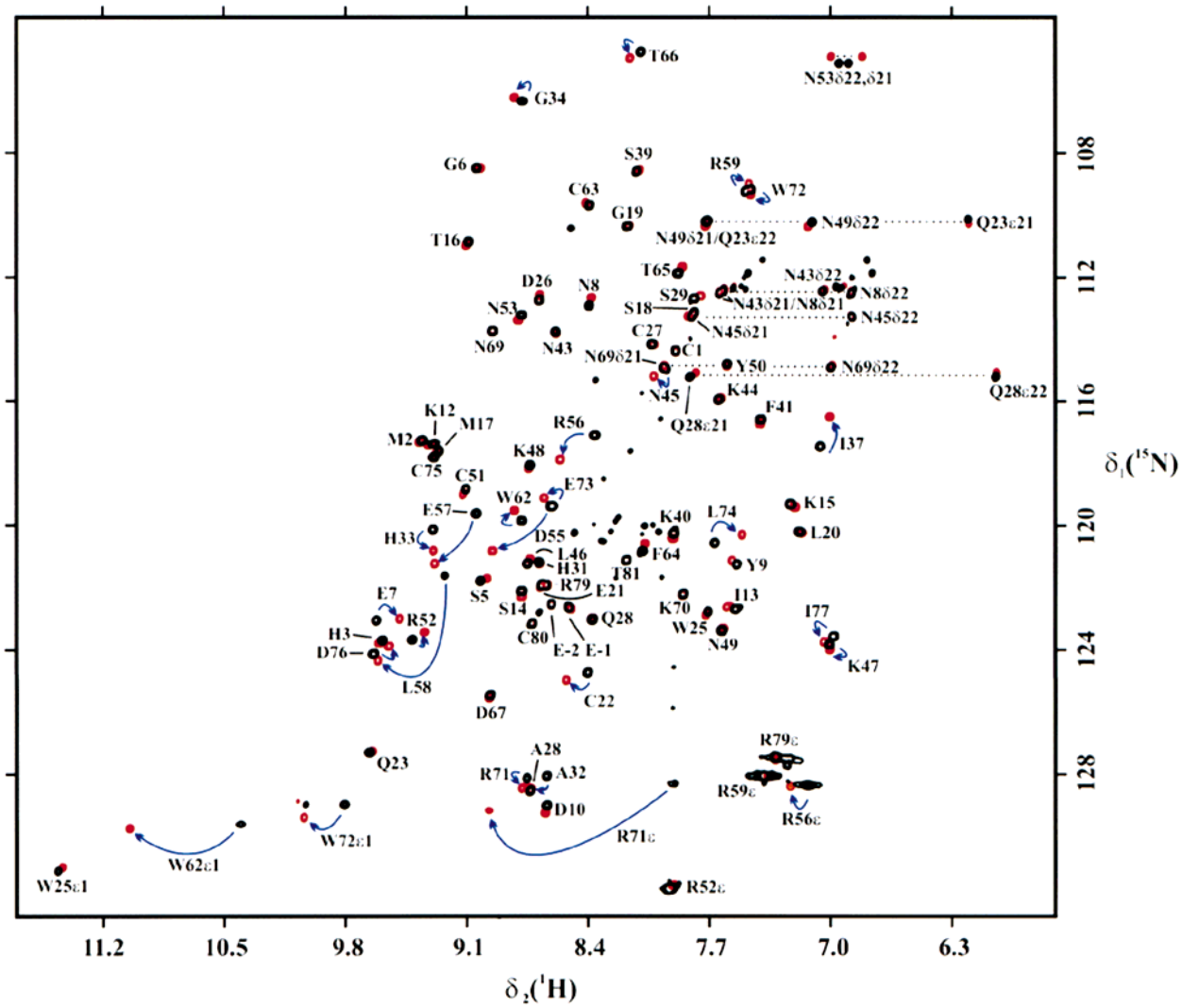

FIGURE 3: $^{1}H-^{15}N$ HSQC spectra of plasminogen kringle 2: the response of NH ^{15}N and ^{1}H resonances to AMCHA binding. Spectra in the absence (black) and presence (red) of a 3-fold molar excess of ligand are shown superimposed. Cross-peaks stemming from Arg NH^{ϵ} groups are folded in δ_1. Most conspicuous ligand-induced, shifted cross-peaks are indicated by blue arrows. Asn $H^{\delta 21}/H^{\delta 22}$ and Gln $H^{\epsilon 21}/H^{\epsilon 22}$ proton pairs, bound to the same $N^{\delta 2}/N^{\epsilon 2}$, are connected by a dotted line. Data were recorded on a 3.2 mM r-K2 sample under the conditions described in the legend of Figure 2.

Table 3: Summary of $^{1}H-^{2}H$ Exchange Data Measured from $^{1}H-^{15}N$ HSQC Cross-Peak Intensities for Kringle 2

ligand-free kringle 2	
8 h[a]	88 h[a]
I13, K15, T16, M17, G19, L20, C22, Q23, W25, S27, S29, K47, N49, Y50, C51, R52, R59, W62, C63, F64, T65, T66, D67, K70, W72, E73, L74, C75, W25 $H^{\epsilon 1}$	I13, W25, R59, W62, C63, F64, W72, E73, L74, C75, Trp25 $H^{\epsilon 1}$
AMCHA-complexed kringle 2 (3:1 AMCHA:K2)	
8 h[a]	186 h[a]
I13, K15, T16, M17, G19, L20, C22, Q23, W25, S27, S29, K47, N49, Y50, C51, R52, E57, R59, W62, C63, F64, T65, T66, D67, K70, W72, E73, L74, C75, W25 $H^{\epsilon 1}$, N53 $H^{\delta 21}$ $H^{\delta 22}$, W62 $H^{\epsilon 1}$	I13, K15, T16, M17, C22, Q23, W25, N49, Y50, C51, R52, R59, W62, C63, F64, T65, T66, W72, E73, L74, C75, W25 $H^{\epsilon 1}$

[a] Time lapsed between dissolving the kringle in $^{2}H_2O$ and completing acquisition of the $^{1}H-^{15}N$ HSQC data.

loops exhibit an intermediate level of definition (rmsd ~ 0.39−0.52 Å).

Pairwise alignment of the N, C^{α}, and C′ backbone skeleton of K2 against those reported for the K1, K4, and K5 crystal structures (*15*, *17*, *72*) yields averaged rmsds of ~1.54, ~1.63, and ~1.58 Å, respectively (Figure 6). A most conspicuous difference is for the His^3-Ser^5 stretches. In K2, the segment contains Cys^4 (mutated to Gly in our r-K2), which forms an interkringle disulfide bond with Cys^{43} of K3. Thus, it is noteworthy that in the r-K2 that is investigated, the Gly^4 $H^{\alpha 3}$ is exposed, which would suggest a similar situation for the Cys^4 side chain in K2, available for generating the interkringle cysteine bridge in the K2+3 supermodule. Furthermore, the segment of residues $Lys^{40}-$

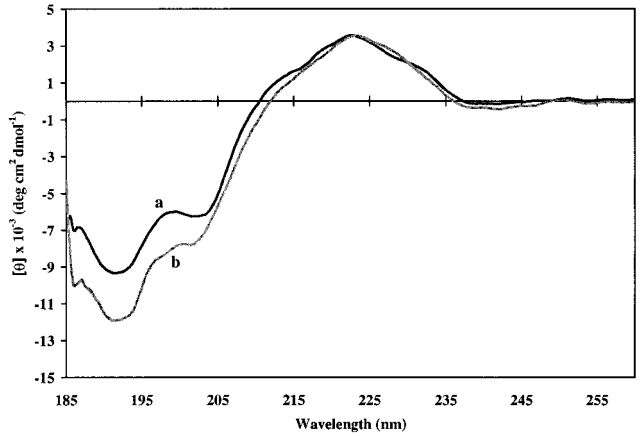

FIGURE 4: Far-UV CD spectra of kringle 2: ligand free (a) and in the presence of a 200-fold molar excess of AMCHA (b). Spectra were recorded on a 2.25 μM r-K2 solution in ^1H_2O at pH 5.13 and 37 °C. Each spectrum represents an average of five scans.

Asn[43] in K2 shows a more open conformation than the corresponding segment in K1, K4, and K5. Interestingly, the backbone dynamics analysis (discussed below) points to increased mobility for the Phe[41] site, which would imply a relatively higher flexibility for this stretch.

Three short antiparallel β-sheets are found in K2 on the basis of backbone atom $^1H-^1H$ NOEs.[4] These pair strands Lys[15]−Thr[16] to Leu[20]−Glu[21], Ala[24]−Trp[25] to Lys[48]−Asn[49], and Trp[62]−Phe[64] to Trp[72]−Leu[74] which are composed of two-, two-, and three-residue pairs, respectively (Figure 5b). β-Sheet amides are characterized by spin−spin couplings ($^3J_{HN\alpha}$) of ≥7 (*58*), as determined for residues 15, 16, 20, 49, 62, and 73 (Figure 7). In K2, ∼80% of the $^{13}C^{\alpha}$ resonances arising from β-sheet residues exhibit characteristic high-field shifts, consistent with statistical criteria (*73*). Expectedly, residues within the β-sheets also exhibit retarded peptidyl amide $^1H-^2H$ exchange rates (Figure 7). Thus, in the Pgn K2, about 18% of the sequence is in β-sheets. An unpaired β-strand, structured by the Pro[30]−Ala[32] segment, is variously identified in 12 of the 20 structures. When combined, the NMR structural data compare reasonably well with the ∼26% β-strand content estimated from the far-UV CD spectra.

Poly(Pro)II-like 3_1-helix, also indicated by the CD data, was identified in K2 on the basis of two criteria: (a) $\phi_i \sim -78°$ and $\psi_i \sim 149°$ (*74*) and (b) $100° < \tau_i < 140°$ and $-150° < \zeta_i < -80°$ (*75*), where τ_i and ζ_i, respectively, are defined as the virtual bond angle $C_\alpha(i-1)-C_\alpha(i)-C_\alpha(i+1)$ and the virtual dihedral angle $O(i-1)=C(i-1)-C(i)=O(i)$. On this basis, the computed NMR structures reveal 3_1-helix for segments Glu[21]−Ala[24] and Leu[74]−Arg[79], with short stretches Tyr[50]−Cys[51], Arg[59]−Pro[61], and Phe[64]−Thr[65] that also satisfy the criteria listed above.

Characterized by short $H^{\alpha}_{(i)}-H^{N}_{(i+2,i+3)}$ and $H^{\alpha}_{(i)}-H^{sc}_{(i+3)}$ distances (*76*), a 3_{10}-helix turn, outlined by residues Pro[38]−Phe[41], was identified from the NOESY data. This concurs with the CD analysis which suggests a 3_{10}-helix content of ∼6%.

Hydrogen Bond Network. The largest β-sheet (Figure 5b), which spans residues Trp[62]−Phe[64] and Trp[72]−Leu[74], is stabilized by the following backbone−backbone H-bond bridges: Cys[63]-NH···OC-Glu[73], Thr[65]-NH···OC-Arg[71], Glu[73]-NH···OC-Cys[63], and Cys[75]-NH···OC-Pro[61]. The sheet exhibits a right-handed twist similar to what is observed for the tPA K2 (*14*) or the uPA kringle (*71*). The two remaining β-structures are each comprised of only four residues, and characterized by similar spatial orientations, being aligned in the same plane. Backbone−backbone hydrogen bonds Ser[14]-CO···HN-Cys[22] and Thr[16]-NH···OC-Leu[20] pair segments Lys[15]−Thr[16] and Leu[20]−Glu[21] in an antiparallel β-sheet. The sheet involving residues Ala[24]−Trp[25] and Lys[48]−Asn[49] is rather sketchy, as only one H-bond, between the peptidyl NH of Trp[25] and the Lys[48] carbonyl, can be identified. All H-bonded amide NHs in β-sheets exhibit retarded $^1H-^2H$ exchange (Figure 7).

β-Sheets of residues 62−64 paired to 72−74 and 15−16 paired to 20−21 are positioned quasi orthogonal relative to each other and connect via a Thr[16]-$H^{\gamma 1}$···O^{ϵ}-Glu[73] H-bond, as found in Pgn K4 and tPA K2 (*77*, *78*). Additional backbone−backbone H-bonds exist between the Met[17] NH and the Leu[74] CO, identified in the Pgn K1, K4, and K5 and tPA K2 and, common to all Pgn kringles, between Gln[23] and Phe[64], neighboring the Cys[22]−Cys[63] bridge (*17*, *72*, *77*, *78*). Unobserved in homologous kringles is the K2 H-bond between the Ser[18] OH^{γ} and the Glu[73] O^{ϵ}. In contrast, while in Pgn K1 Lys[15] interacts with Asp[76] (*16*), only one of the 20 K2 structures displays H-bonding between the two side chains.

The 3_{10}-helix turn involves H-bonds between $CO_{(i)}$ and $NH_{(i+3)}$, specifically between Ile[37]-CO···HN-Lys[40] and Pro[38]-CO···HN-Phe[41], the former also identified in the Pgn K1 and K5 (*17*, *72*). Pro[38] satisfies the 3_{10}-helix criterion of displaying a ϕ of about −49° and a ψ of about −26°, whereas the following two residues exhibit increasing deviations from the idealized values. In the Pgn K1−AMCHA complex (*17*), tPA K2 (*78*), and the uPA kringle (*71*), short helices of about one to two turns have been identified which, when compared against K2, are shifted downstream by two to four residues. Four β-turns are indicated,[5] encompassing segments Gly[6]−Tyr[9] (1), Thr[16]−Gly[19] (2), Asn[53]−Arg[56] (3), and Asp[67]−Lys[70] (4), characterized by a $CO_{(i)}$···$HN_{(i+3)}$ hydrogen bond. These H-bonds and β-turns are also observed in the Pgn K1, K4, and K5, except for the H-bond between residues 53 and 56, which is missing in K4 (*17*, *72*, *77*).

[4] NOESY connectivities which confirm the first β-sheet were identified between proton pairs Lys[15] H^{α} and Cys[22] H^N, Lys[15] H^{α} and Glu[21] H^{α}, Thr[16] H^N and Glu[21] H^{α}, and Thr[16] H^N and Leu[20] H^N. The second β-sheet involves a total of four residues; however, the structure yields only two NOE connectivities: between Ala[24] H^{α} and Asn[49] H^{α} and between Trp[25] H^N and Asn[49] H^{α}. The third β-sheet displays the following NOE connectivities: between Trp[62] H^{α} and Cys[75] H^N, between Trp[62] H^{α} and Leu[74] H^{α}, between Cys[63] H^N and Leu[74] H^{α}, between Cys[63] H^N and Glu[73] H^N, between Phe[64] H^{α} and Glu[73] H^N, betweeen Thr[65] H^N and Trp[72] H^{α}, and between Thr[65] H^N and Arg[71] H^N.

[5] Based on the following NOE connectivities: (1) Glu[7] H^N-H^N Asn[8], Glu[7] $H^{\alpha}-H^N$ Tyr[9], and Asn[8] H^N-H^N Tyr[9], (2) Met[17] H^N-H^N Ser[18], Met[17] $H^{\alpha}-H^N$ Ser[18], Met[17] $H^{\alpha}-H^N$ Gly[19], and Ser[18] H^N-H^N Gly[19], (3) Pro[54] $H^{\alpha}-H^N$ Asp[55] and Asp[55] H^N-H^N Arg[56], and (4) Pro[68] $H^{\alpha}-H^N$ Asn[69], Pro[68] $H^{\alpha}-H^N$ Lys[70], and Asn[69] H^N-H^N Lys[70].

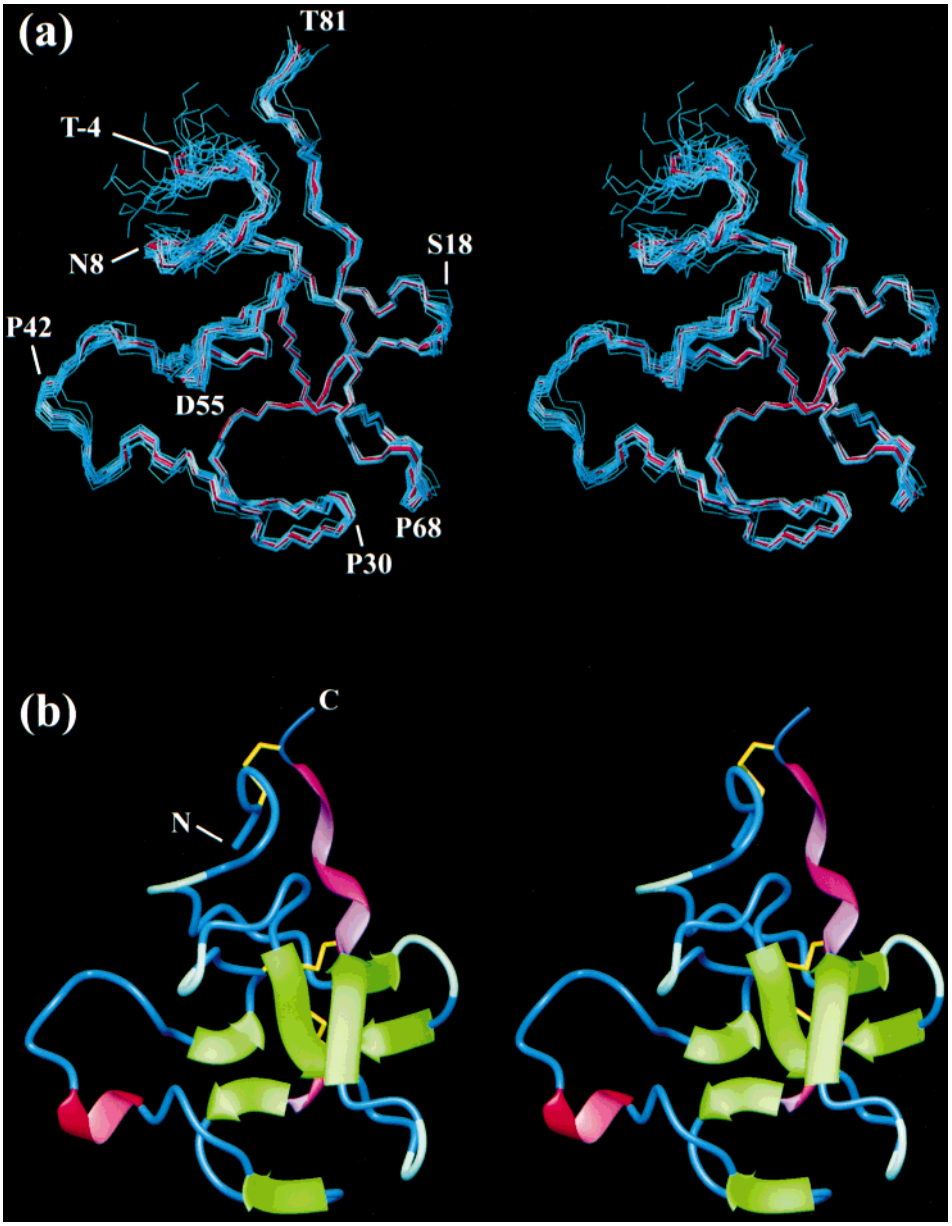

FIGURE 5: Stereoviews of kringle 2 NMR structures. (a) Skeleton of 20 selected structures (blue) superimposed by fitting backbone (N, C^{α}, and C′) atoms to the computed mean (red). Positions of selected residues are indicated. (b) Representative model. Secondary structure elements are highlighted in ribbon representation: turn of 3_{10}-helix (red), 3_1-helix (pink), and β-strands (green). β-Turns and disulfide bonds are represented as light blue and yellow traces, respectively. Both displays correspond to a frontal view of the ligand binding site. The figures were generated with the program MOLMOL-2.6 (*63*).

The Trp^{25} $NH^{\epsilon 1}$, which exhibits the slowest $^1H-^2H$ exchange kinetics among Trp indole groups in K2, is H-bonded to the Tyr^{50} CO, while its backbone NH H-bonds the Lys^{48} CO. The two H-bonds are also found in Pgn K1, K4, and K5 and the tPA K2. Furthermore, the Trp^{62} $NH^{\epsilon 1}$ is H-bonded to the Asp^{55} CO^{δ}, whereas the corresponding group of Trp^{72} is not involved in H-bond formation, consistent with its fast $^1H-^2H$ exchange.

Hydrophobic Core and Binding Site. The K2 ligand binding site was identified on the basis of 28 unambiguous kringle−ligand NOEs (Figure 8a and Table 2). The ligand is in close vdW contact with the aromatic rings of Trp^{62} and Trp^{72}, oriented at ∼75° relative to each other (Figure 8b,c). In the K2 ^1H NMR spectrum, the Trp^{72} indole $H^{\zeta 3}$ resonance appears at 6.43 ppm, while in the Pgn K4 and tPA K2 spectra, the equivalent signals exhibit distinct high-field shifts (5.03 and 5.51 ppm, respectively) (*14*, *79*). In both the Pgn K4 and tPA K2, position 74 is occupied by a Tyr residue whose ring H^{δ} and H^{ϵ} protons are separated from the Trp^{72} $H^{\zeta 3}$ by ∼3.7−4.7 Å, the Tyr^{74} aromatic ring inducing high-field shifts on the Trp^{72} $H^{\zeta 3}$ resonance. In contrast, K2 carries a Leu residue at position 74, also close to the Trp^{72} $H^{\zeta 3}$. Thus, the K2 Trp^{72} indole spectrum is typical of an exposed, "random coil" Trp side chain.

Tyr^{36} exhibits NOE connectivities to Trp^{25}, Trp^{62}, and Phe^{64}. The latter, in turn, interacts with the Trp^{25}, Tyr^{36}, Trp^{62}, and Trp^{72} side chains, with Trp^{25} exhibiting NOE connectivity to Trp^{62}. Thus, Trp^{25}, buried within the K2 structure, expectedly does not exhibit Overhauser connectivities to the ligand. Likewise, Leu^{46}, whose δ-methyl resonances exhibit a high-field shift (−0.85 and 0.48 ppm), a fingerprint of a proper kringle fold, is not in contact with the ligand. NOE connectivities between the Leu^{46} $H^{\delta 1}$ and $H^{\delta 2}$ and the Trp^{25} indole ring and Phe^{41} side chain localizes the strictly

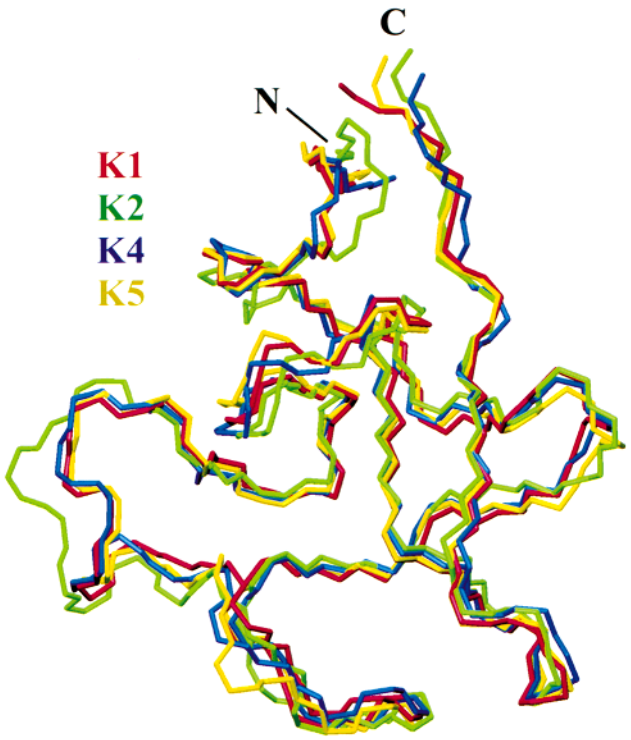

FIGURE 6: Backbone (N, C^{α}, and C′) alignment of the kringle 2 solution structure (green) against homologous plasminogen kringle crystallographic structures: K1, red; K4, blue; and K5, yellow. K1 and K4 represent structures complexed with AMCHA and 6-AHA, respectively (*15*, *17*), whereas K5 is ligand-free (*72*).

conserved Leu^{46} residue at the center of the hydrophobic core underlying the ligand binding site.

Molecular Dynamics. ^{15}N magnetic relaxation and $^{1}H-^{15}N$ NOE data for the K2 backbone amides are summarized in Figure 10. Within the K2 structure proper (residues $Cys^{1}-Cys^{80}$), the average T_1 and T_2 are 0.40 and 0.16 s, respectively.[6] In the $^{1}H-^{15}N$ XNOE experiment, residues exhibiting the most pronounced response to proton rf saturation are Glu^{-2}, Glu^{-1}, Cys^{1}, Lys^{47}, Arg^{56}, Ile^{77}, Arg^{79}, and Thr^{81}. In the case of side chain NH^{ϵ} groups, the (folded) cross-peaks from Arg residues 56 and 79 change the sign in the proton saturation experiment, consistent with high mobility, whereas Arg^{52}, Arg^{59}, and Arg^{71} exhibit weaker responses (intensity ratios of 0.63, 0.14, and 0.60, respectively), suggesting a degree of immobilization.

Magnetic relaxation experiments with the K2−AMCHA complex were analyzed according to the extended Model-Free approach (*66*, *67*). From the data, a τ_c of ∼4.49 ns was estimated. In general, most residues within the K2 sequence exhibit backbone order parameters S^2 in the range of 0.8−0.9, indicative of a structurally well defined domain. Chemical exchange terms R_{ex} were fitted for residues C22, H31, H33, I37, T65, T66, and W72. Excluding N- and C-terminal tails ($0.45 < S^2 < 0.61$), the overall generalized order parameter for K2 is 0.85 ± 0.04. For residues within the $Asn^{69}-Lys^{70}$ and $Asp^{76}-Cys^{80}$ segments, relatively lower values of S^2 are determined ($\langle S^2\rangle \sim 0.79$ and 0.76, respectively; Lys^{70} 0.76, Ile^{77} 0.66, and Arg^{79} 0.76). Additional K2 residues characterized by relatively low order parameters are Cys^{1} (0.71), Ser^{5} (0.79), Lys^{12} (0.80), Glu^{21} (0.76), Ser^{27} (0.78), Phe^{41} (0.77), and Lys^{47} (0.69). Within the loops (seven total), $\langle S^2\rangle$ ranges between 0.78 and 0.87. The least mobile peptide segments (picosecond time scale) are those encompassing the two inner disulfide bonds ($\langle S^2\rangle \sim 0.86-0.87 \pm 0.03$): loops 51−63 and 63−75.

Similarly, segments participating in antiparallel β-sheets are characterized by low mobility. Thus, paired stretches 15−16 to 20−21, 24−25 to 48−49, and 62−64 to 72−74 exhibit high $\langle S^2\rangle$ values, namely, ∼0.84, ∼0.87, and ∼0.89, respectively. The latter β-sheet includes Trp^{62}, the residue exhibiting the highest backbone S^2 in K2 (∼0.95 ± 0.014). Two backbone amide H-bonds are observed between Arg^{52} and Trp^{62} which might restrict its mobility. These results are in line with the assessment that Trp^{62} can contribute significantly to the stability of the native kringle conformation (*83*). The alternating high and low values of S^2 for the $Cys^{63}-Asp^{67}$ segment reflect localized H-bonding. The more ordered Cys^{63}, Thr^{65}, and Asp^{67} NH groups bind Glu^{73} and Arg^{71} backbone CO groups and Thr^{65} $O^{\gamma 1}$, respectively, whereas the Phe^{64} and Thr^{66} NHs exhibit no H-bonding. Amide NH groups of key residues at the binding site ionic centers (Asp^{55}, Glu^{57}, and Arg^{71}) generally are endowed with low mobility ($S^2 \sim 0.88$, 0.86, and 0.91, respectively). Residues with relatively unordered backbone peptidyl bonds such as Ser^{5}, Glu^{21}, Lys^{47}, and Ile^{77} are characterized by non-H-bonded amide NH groups.

In case of side chains, S^2 values of ∼0.79 are obtained for Trp^{25} and Trp^{62} $NH^{\epsilon 1}$ groups, somewhat higher than that for Trp^{72} (0.72). These S^2 values are consistent with the Trp^{25} and Trp^{62} $NH^{\epsilon 1}$ groups being internally H-bonded and exhibiting retarded $^{1}H-^{2}H$ exchange in $^{2}H_2O$. The S^2 values of the Arg^{52}, Arg^{59}, and Arg^{71} NH^{ϵ} groups, which show a positive peak intensity ratio in the XNOE experiment, were determined to be 0.75, 0.46, and 0.64, respectively. It is likely that the values reflect the extent of H-bonding; in the 20 calculated final structures, Arg^{52} NH^{ϵ} interacts with Asn^{45} CO (in 14 out of 20 structures), the Arg^{59} NH^{ϵ} is H-bonded to Cys^{75} CO (5 out of 20), and the NH^{ϵ} of Arg^{71} is H-bonded to the ligand's carboxylate group (11 out of 20). The latter result would be consistent with the mobility of the Arg^{71} side chain decreasing upon ligand complexation.

DISCUSSION

The structures of ligand-complexed tPA K2, Pgn K1, K4, and K5 have been characterized by NMR and X-ray crystallographic methods (*14*−*17*, *87*). From these studies, the binding site has been identified as being configured by residues 35, 36, 55−57, 62−64, and 71−74 (*19*, *71*, *72*, *77*, *78*, *88*). Backbone alignment of Pgn K1, K2, K4, and K5 (Figure 6) shows that the four lysine-binding kringles in Pgn exhibit similar overall foldings. On the other hand, the reported (*30*) NOE connectivities between 6-AHA and K2 indicate close van der Waals contacts of the ligand with the

[6] Within the kringle proper, the residues with T_1 values exceeding the average are Ser^{5} (0.43 s), Lys^{12} (0.42 s), Glu^{21} (0.44 s), Ser^{27} (0.44 s), His^{31} (0.42 s), Phe^{41} (0.43 s), Lys^{47} (0.48 s), Asn^{53} (0.42 s), Asn^{69} (0.42 s), Lys^{70} (0.44 s), and Ile^{77} (0.50 s). Residues with T_2 values distinctly larger than those of their neighbors are Ser^{5} (0.18 s), Glu^{21} (0.19 s), Lys^{47} (0.20 s), Lys^{70} (0.19 s), and Ile^{77} (0.23 s), while significantly short T_2 values characterize residues His^{31} (0.08 s), His^{33} (0.1 s), and Ile^{37}, Thr^{65}, and Thr^{66} (0.12 s). Expectedly, larger T_1 (T_2) values result for residues within the Glu^{-2}-Glu^{-1}-Cys^{1} N-terminal tail as well as for the C-terminus, Thr^{81}: Glu^{-2}, 0.58(0.38) s; Glu^{-1}, 0.50(0.28) s; Cys^{1}, 0.46(0.22) s; and Thr^{81}, 0.47(0.24) s.

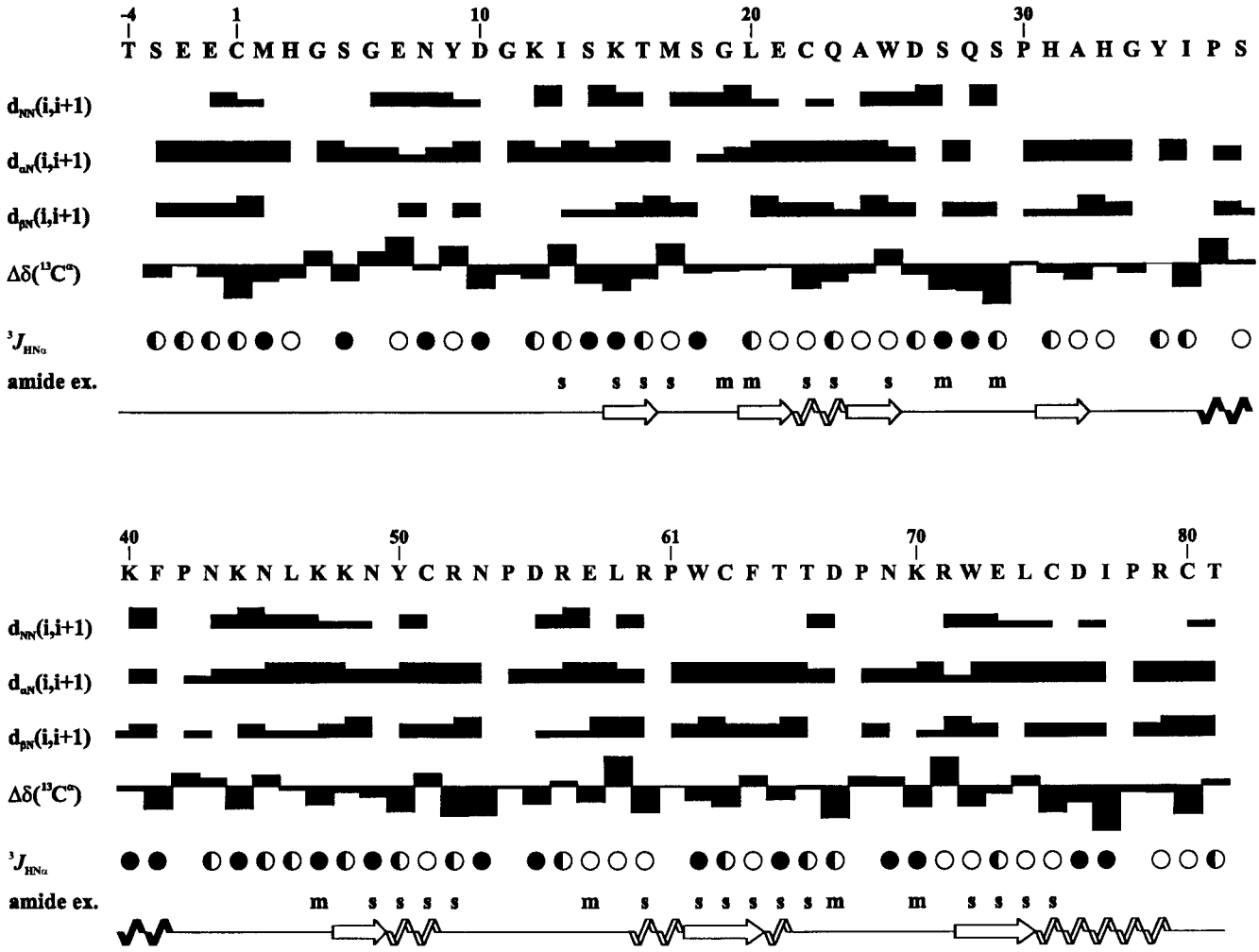

FIGURE 7: Summary of kringle 2 NMR sequential connectivities, $^{13}C^{\alpha}$ chemical shift changes, $^{3}J_{HN\alpha}$ couplings, and amide $^{1}H-^{2}H$ exchange kinetics. Sequential NOEs between $H^{N}_{(i+1)}$ and $H^{N}_{(i)}$, $H^{N}_{(i+1)}$ and $H^{\alpha}_{(i)}$, and $H^{N}_{(i+1)}$ and $H^{\beta}_{(i)}$, respectively, were measured at pH* 5.1 and 37 °C via a three-dimensional ^{15}N-edited NOESY-HSQC experiment with τ_{mix} of 150 ms. The relative intensities of NOE cross-peaks are indicated by the widths of the bars. $^{13}C^{\alpha}$ chemical shifts were determined via an HNCA experiment. Bars represent the change in chemical shift relative to the random coil $^{13}C^{\alpha}$ shift (*73*). $H^{N}-H^{\alpha}$ couplings, extracted from the HNHA experiment, are denoted by empty ($^{3}J_{HN\alpha}$ < 6 Hz), half-filled (6 Hz ≤ $^{3}J_{HN\alpha}$ ≤ 8 Hz), and filled ($^{3}J_{HN\alpha}$ > 8 Hz) circles. Peptidyl amide protons, yielding cross-peaks in the $^{1}H-^{15}N$ HSQC experiment 8 and 186 h after dissolving r-K2 in $^{2}H_{2}O$, are classified as being of medium (m) and slow (s) exchange rates, respectively. Data were extracted from experiments with the AMCHA-complexed r-K2. The kringle's primary and secondary structures are shown; arrows denote β-sheet strands and empty and filled zigzag lines 3_1- and 3_{10}-helical segments, respectively.

aromatic side chain rings of residues Tyr[36], Trp[62], Phe[64], and Trp[72], in agreement with those previously measured between various ligands and the homologous kringles. Therefore, other specific differences in the constellation of residues at the LBS are expected to modulate their relative affinities toward small zwitterionic ligands (*30*). By reference to the homologues, the putative Pgn K2 binding site exhibits (a) a Glu instead of an Asp residue at position 57, (b) a basic residue, Arg[56], between Asp[55] and Glu[57], and (c) a lack of a basic residue at position 35. Furthermore, K2 is devoid of Tyr[74] (replaced by Leu[74]) which in the homologous Pgn kringles stabilizes the orientation of the aromatic ring of residue 72 at the LBS.

The antifibrinolytic agent AMCHA, among the most potent kringle ligands, is characterized by the following equilibrium association constants: K_a > 300 mM^{-1} for Pgn K1 (*84*), ~159 mM^{-1} for Pgn K4 (*85*), ~44.2 mM^{-1} for Pgn K5 (*25*, *30*), and ~69.4 mM^{-1} for tPA K2 (*86*). By comparison, the affinity of the Pgn K2 for AMCHA (K_a ~ 7.3 mM^{-1}) is relatively low (*30*). The $^{1}H-^{15}N$ HSQC experiments (Figure 3) reveal that it is the Asp[55]−Leu[58] peptide backbone segment that exhibits the highest response to AMCHA binding (Figure 9). Within this segment, the Leu[58] amide resonances display the most pronounced ligand-induced shift, echoing perturbation of the Glu[57] $^{\delta}COO^{-}$, to which it is H-bonded. These effects are consistent with the canonical kringle LBS model, which attributes key roles to the acidic residues at positions 55 and 57 in the interaction with ligand (*81*). Backbone amides of LBS residues such as Trp[62], Phe[64], Arg[71], and Trp[72] are less affected by the ligand, in line with structural stabilization within a β-sheet. Revealing close proximity of K2 aromatic rings to the ligand, indole group NHs of Trp[62] and Trp[72] are substantially perturbed by AMCHA.

The modeled electrostatic surface potential of the ligand binding site is shown in Figure 8d. A NOESY cross-peak linking the AMCHA H_{32} to the Glu[57] H^{β} (Figure 8a) constrains the ligand's amino group to becoming positioned within ionic interaction distance with the carboxylate group of Asp[55] and Glu[57] (Figure 8b). In the 20 K2 structures, the cationic AMCHA amino group results placed either close to the Glu[57] δ-carboxylate group (12 out of 20), close to the Asp[55] γ-carboxylate group (4 out of 20), or between the two

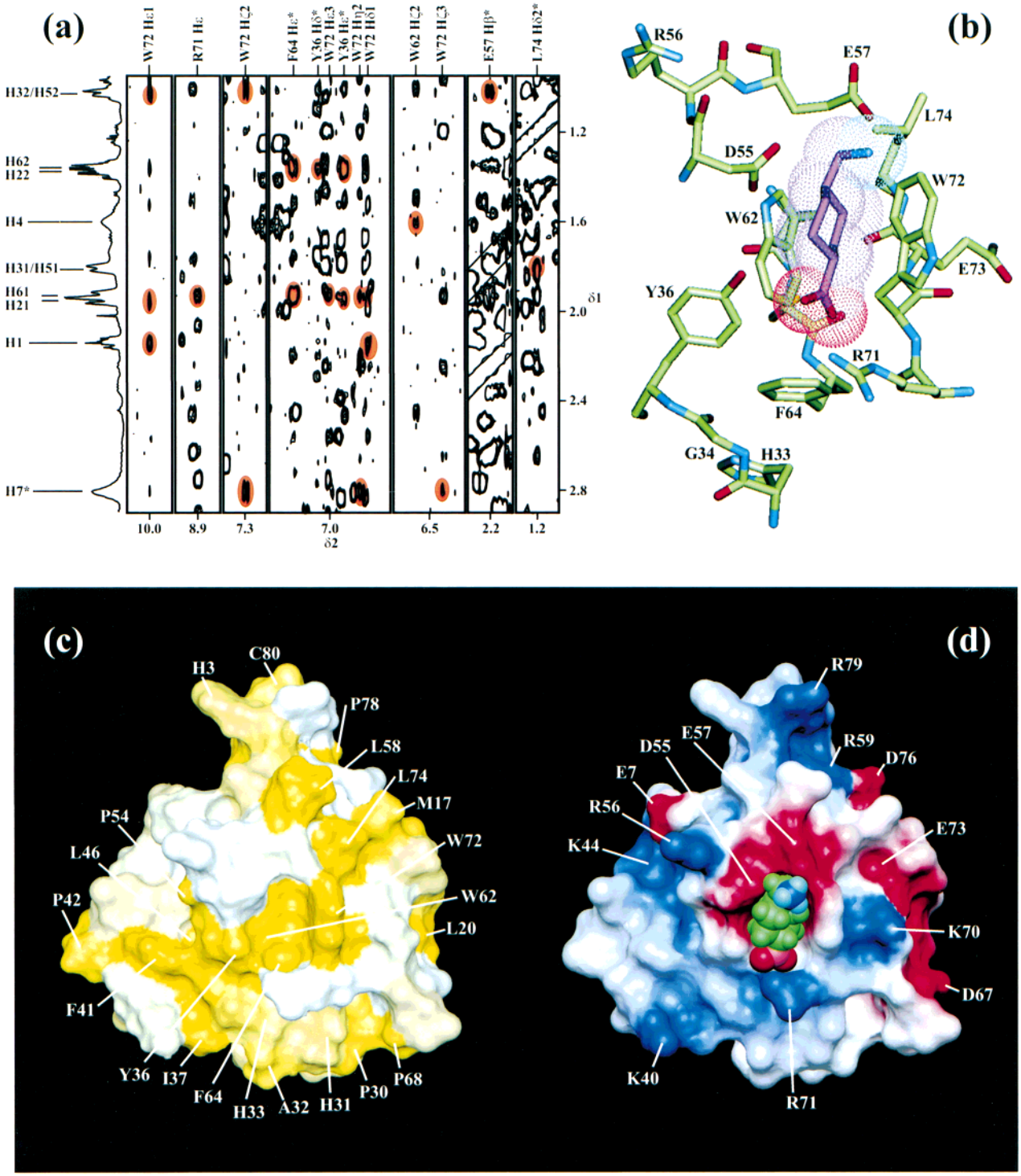

FIGURE 8: AMCHA−kringle 2 ^{1}H NMR NOESY connectivities and structure of the kringle 2 ligand binding site. (a) Intermolecular NOESY cross-peaks are highlighted in orange. The spectrum was recorded at a r-K2:AMCHA ratio of 1:15 with a τ_{mix} of 250 ms. Experimental conditions are as described in the legend of Figure 3. The one-dimensional AMCHA spectrum is shown on the left. (b) Residue segments His^{33}−Tyr^{36}, Asp^{55}−Glu^{57}, Trp^{62}−Phe^{64}, and Arg^{71}−Leu^{74} of the K2 binding site are displayed. The AMCHA backbone is colored magenta; N and O atoms are blue and red, respectively. AMCHA was docked by incorporating 28 K2−ligand NOE distance constraints in the structure calculation (Table 2). (c) The kringle surface is colored in increasing grades of yellow, in proportion to the hydrophobicity of the amino acid side chains (*80*). (d) Electrostatic surface potential of K2. Negatively and positively charged areas are red and blue, respectively. The backbone of the ligand AMCHA is shown in green. The spatial orientation of the molecule in panels c and d is identical. The illustrations were generated with Quanta96 (Molecular Simulations Inc.) (b) and MOLMOL-2.6 (*63*) (c and d).

anionic groups (4 out of 20). Thus, on average, the applied force field would place the AMCHA N atom relatively closer to the COO^- group of Glu^{57} (∼3.9 Å) than to that of Asp^{55} (∼4.4 Å) which, in turn, is H-bonded to Trp^{62} H$^{\epsilon 1}$. On the basis of chemical modification experiments, ligand preference for the anionic side chain at position 57 had been indicated for K4 by Patthy and co-workers (*82*). In addition, the Glu occupancy of position 57 results in the side chain carboxylate group showing a relatively lower degree of alignment along the longitudinal axis of the binding site than is the case for the Asp^{57} side chain in the homologous Pgn kringles, which would lead to an entropically less favorable interaction with

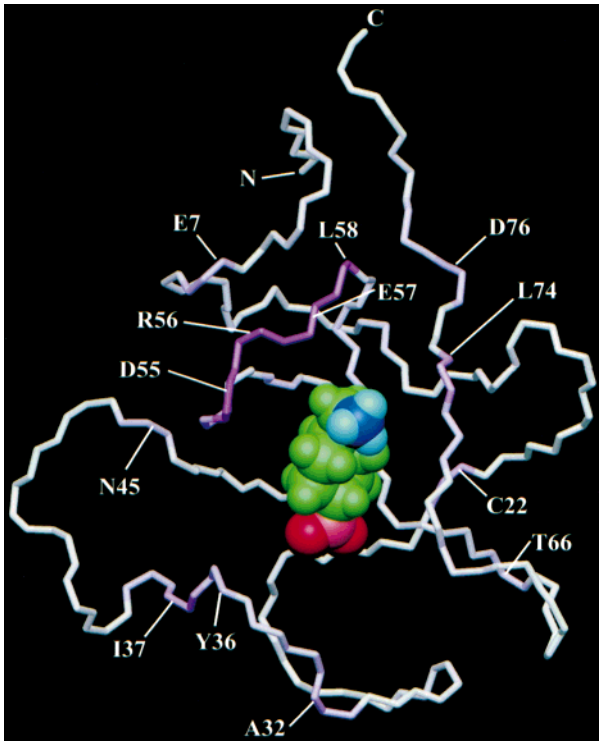

FIGURE 9: Ligand binding as demonstrated by AMCHA-induced chemical shift changes of kringle 2 backbone $^{1}H-^{15}N$ resonances. The hydrocarbon backbone of AMCHA is displayed (green). Most affected residues upon ligand complexation are indicated; the color intensity (purple) is proportional to the response of cross-peaks in $^{1}H-^{15}N$ HSQC spectra (Figure 3) to ligand addition. This figure was generated with MOLMOL-2.6 (*63*).

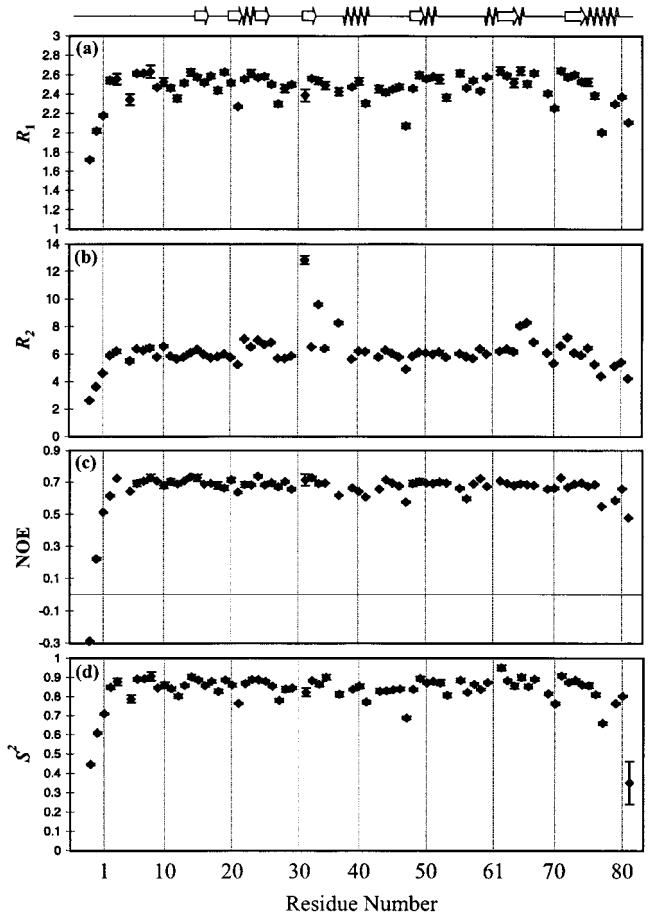

FIGURE 10: Sequence profile of backbone spin relaxation and order parameter data for the kringle 2−AMCHA complex. (a) R_1 is the inverse of the backbone ^{15}N T_1, (b) R_2 the inverse of the backbone ^{15}N T_2, and (c) NOE the heteronuclear $^{1}H-^{15}N$ NOE intensity ratio, and (d) the generalized order parameters S^2 are computed on the basis of the extended model-free approach (*66*, *67*). The K2 secondary structure is outlined at the top.

the ligand's cationic group. Also, the crystallographic structures of ligand-complexed K1 and K4 show the Asp^{55} and Asp^{57} C^{γ} atoms to be separated by ~5.2 Å, while in the K2 NMR structure, the corresponding $Asp^{55}-Glu^{57}$ $C^{\gamma}-C^{\delta}$ distance is ~5.7 Å.

In the homologous Pgn kringles, an electrostatically neutral residue occupies position 56, i.e., sandwiched between Asp^{55} and Asp^{57}. In K2, the Arg^{56} guanidinium group is poised to ion-pair the Glu^{7} $^{\delta}COO^{-}$. Coincidentally, as revealed by the HSQC experiment (Figure 3), the Glu^{7} NH is sensitive to the presence of AMCHA. Hence, the Arg^{56} cationic locus, although electrostatically might weaken the interaction with ligand, is unlikely to directly interfere with the binding. As shown elsewhere (*30*), a double Arg56Gly/Glu57Asp mutation only marginally increases the affinity of K2 for ligand.

The HSQC experiment (Figure 3) is consistent with the Trp^{62} and Trp^{72} indole rings interacting with AMCHA. Concurrently, the spectra provide novel unambiguous evidence for the Arg^{71} guanidinium group mediating ligand binding, as previously claimed for the Pgn K1 and K4 (*15*, *16*, *82*). The drastic shift of the K2 Arg^{71} NH^{ϵ} ^{1}H and ^{15}N resonances to low fields (notice that the Arg^{71} NH^{ϵ} cross-peak is folded along δ_1) concurs with the generation of a significant H-bond, purportedly via electrostatic interaction of the Arg^{71} cationic group with the carboxylate group (distances to N^{η} and N^{ϵ} of ~3.0 and ~4.1 Å, respectively; Figure 8b) of the ligand which, in turn, is also H-bonded to Tyr^{36} OH^{η}. Finally, the positive electrostatic potential at the southern end of the lysine binding site is further strengthened by an alignment of the His^{31} and His^{33} imidazole groups, the latter stacked against the Phe^{64} (Tyr^{64} in K1) aromatic ring.

The negative and positive ionic centers of the binding site position themselves ~1 Å closer in K2 than in the homologous K1 or K4. Conceivably, this may be related to the Arg^{71} side chain in K2 not being restricted by an H-bond to the backbone CO of the position 32 residue or by electrostatic repulsion from a basic side chain at position 35, as is the case for Arg^{71} in K1 and K4. Thus, while in the K1−AMCHA complex the Arg^{71} $N^{\eta 2}$ is separated from Asp^{55} and Asp^{57} O^{δ} atoms by ~10.0 and ~12.1 Å, respectively, and in the K4−6AHA complex by ~9.4 and ~12.5 Å, respectively, somewhat shorter distances, ~8.3 and ~10.8 Å, respectively, result between the corresponding atoms in the K2−AMCHA complex. This would be consistent with the anomalous preference of K2 for 5-APA over 6-AHA, a one-methylene unit (~1.14 Å) longer ligand (*30*).

Paralleling what is observed for AMCHA, the ligand N^{α}-acetyl-L-lysine exhibits ~40-fold weaker interaction for the Pgn K2 (K_a ~ 0.96 mM^{-1}) than for K1 and K4 (K_a ~ 41 and 37 mM^{-1}, respectively). In contrast, N^{α}-acetyl-L-lysine methyl ester, which lacks a free carboxylate group, exhibits similar binding affinities for K1, K2, and K4 (K_a ~ 0.16, 0.1, and 0.2 mM^{-1}, respectively) (*30*). Thus, when compared against those of the Pgn K1 and K4, the interaction of K2

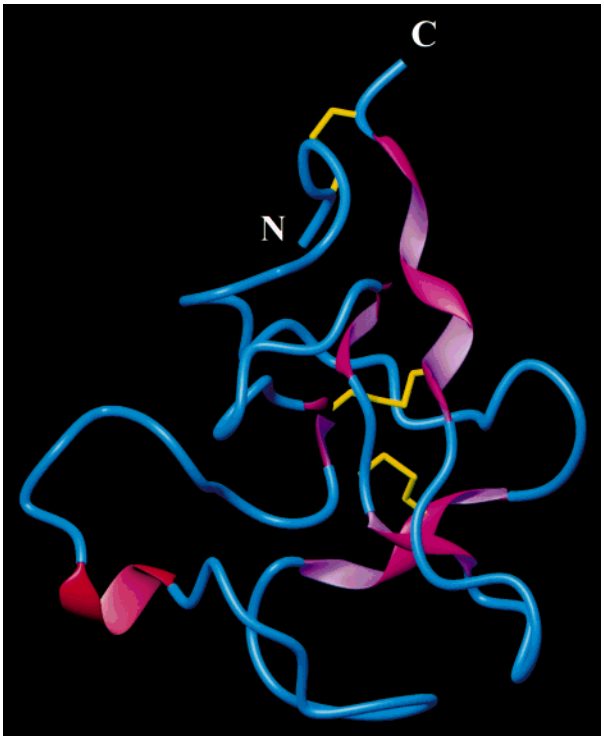

FIGURE 11: Helix components in the kringle 2 structure. The helices are highlighted in ribbon representation: 3_1-helix (pink) and 3_{10}-helix (red). Disulfide bonds are yellow.

with zwitterionic ligands is suggested also to be weakened by a less supportive ion pairing configuration of the cationic center at the binding site (Figure 8b−d). Indeed, besides the different orientation of the Arg[71] guanidino group in both K1 and K4, in these kringles the positive electrostatic potential is boosted by the contribution of the Arg[35] (K1) or Lys[35] (K4) side chains.

An unforeseen result stemming from this study is the uncovering of significant 3_1-helix in the structure of human Pgn K2. The extended left-handed 3_1-helix motif, with three residues per turn, is not characterized by a pattern of internal H-bonds as the peptidyl N−H and C═O bonds project outward. Hence, recognition of 3_1-helix by visual inspection of the structure is cumbersome, which explains the infrequent identification of such helices in reported protein structures (*74*, *89*). Furthermore, direct assessment of 3_1-helix structure from homonuclear ^{1}H NOE connectivity criteria may in general prove to be difficult to accomplish; as measured from a computer-generated model of (poly)Ala in a 3_1-helix conformation, the closest interproton distances are as follows: $d_{H^N(i)-H^N(i+1)} = 4.69$ Å, $d_{H^N(i)-H^\alpha(i+1)} = 5.56$ Å, $d_{H^\alpha(i)-H^N(i+1)} = 2.15$ Å, $d_{H^\alpha(i)-H^\alpha(i+1)} = 4.32$ Å, $d_{H^\alpha(i)-H^\beta(i+1)} = 4.05$ Å, and $d_{H^\beta(i)-H^\beta(i+1)} = 4.82$ Å. It follows that the only interproton distances shorter than 6 Å are sequential and, therefore, not particularly informative. In contrast, the far-UV CD spectrum, being most sensitive to secondary structure, readily detects 3_1-helix regularity (*75*).

CD spectroscopy has been found useful for a qualitative assessment of kringle β-structure content (*90*, *91*). A significant presence of 3_1-helix in the structure of human Pgn K2 was indicated from analysis of the far-UV CD spectra of K2 (Figure 4) using CDsstr, a recently released computer program (*32*). The CD results motivated us to re-examine the atomic coordinates of the 20 selected K2 NMR structures via an objective search (*89*). This led us to identifying segments Glu[21]−Ala[24] and Leu[74]−Arg[79], as well as dipeptide stretches Tyr[50]−Cys[51], Arg[59]−Pro[61], and Phe[64]−Thr[65], as consistently satisfying the criteria for 3_1-helix (Figure 11).

Since 3_1-helix had been ignored in the secondary structure analysis of previous NMR and X-ray crystallographic models of kringles, prompted by the CD analysis of K2, we have inspected reported structures of Pgn (*16*, *17*, *72*, *77*, *92*), apolipoprotein(a) (*93*), hepatocyte growth factor (*94*), and prothrombin kringles (*95*, *96*), which are available from the Brookhaven Protein Data Bank, as these modules belong to the same family (*78*, *81*). Using XTLsstr (*89*), we find that the homologous three-dimensional structures also exhibit closely alignable segments which share with the Pgn K2 3_1-helix characteristics. From inspection of Figure 12, it is apparent that 3_1-helical segments tend to cluster around Cys

```
                    1        10        20        30        40        50        60        70        80
                    |        |         |         |         |         |         |         |         |
Pgn K1              C------------------TCQK---------*--------------YCR--------PWCYT---------C--LEC (X)
Pgn K1 (6-AHA)      C------------------ITCQK---------*--------------YC-----------C----------YC--LEC (X)
Pgn K1 (6-AHA)      C--------------------C-----------*-FSP-----------C-----------C-----------C-IL-C (N)
Pgn K1 (AMCHA)      C------------------ITC-----------*--------------YC-----------CYT--------YC--LEC (X)
Pgn K2 (AMCHA)      C--------------------ECQA----------*--------------YC-------R*P-CFT--------LC--PRC (N)
Pgn K4              C------------------KKCQS----------*-------------YC------*----CFT--------YC----C (X)
Pgn K4 (6-AHA)      C------------------KCQS----------*-------------YC------*----C----------YC-LK-C (X)
Pgn K5              C------------------TPCQD-------------------------YC-----------CYT---------C--PQC (X)
APO K4 (6-AHA)      CYH----------------RTCQS----------*-------------YC------*----CFT--------YC--TRC (X)
HGF K1              C------------------IKCQP---------*--------------YC-----EE----CFT--------VC--PQC (X)
BPt K1              C------------------IECQL-------------*-----------C-----------C----------ECSVPVC (X)
HPt K2              C--------------------PCLA-------------*-FN--------FC---------VWC----KP----YCDLNYC (X)
```

FIGURE 12: Homologous kringles with known structure and the location of the 3_1-helix. (N) denotes the NMR structure (*16*) and (X) the X-ray structure (*15*, *17*, *72*, *77*, *92*−*96*). When the structure is for a kringle−ligand complex, the ligand is indicated in parentheses. APO, human apolipoprotein(a) (*93*); BPt, bovine prothrombin (*95*); HGF, human hepatocyte growth factor (*94*); HPt, human prothrombin (*96*); Pgn, human plasminogen (*15*−*17*, *72*, *77*, *92*). Conserved Cys residues, participating in cystine bridges, are denoted with a C. Only residues participating in 3_1-helix structure are explicitly included (bold characters). A star denotes deletions, necessary for proper alignment, by reference to the Pgn K5 sequence.

residues 22, 51, 63, 75, and 80, with stretches of residues 20−24 and 74−80 statistically contributing most of the 3_1-helix content. From this analysis, we are led to conclude that 3_1-helix indeed is an important component of kringle secondary structure, to the extent that in the human prothrombin K2 22.8% of the sequence configures 3_1-helices, surpassing its 17.7% β-sheet content.

Despite the structural constraints imposed by the Cys^{51}−Cys^{75} and Cys^{1}−Cys^{80} bridges, the segment of residues 75−80 is the least ordered within the K2 structure ($\langle S^2 \rangle \sim 0.78 \pm 0.05$). Coincidentally, this stretch contains most of the Leu^{74}−Arg^{79} 3_1-helix, in agreement with the assessment that 3_1-helices are intrinsically flexible and prone to dynamically interconvert to other types of secondary structure (*74*). Thus, one may ponder whether some sort of "accordion" stretch or compression dynamics at this disulfide-bridged segment may not reflect a functional adaptability of kringle modules to interact with macrosubstrate ligands, such as fibrin(ogen), receptors, and extracellular matrix proteins.

CONCLUSIONS

The Pgn K2+3 construct is evolutionary conserved all the way from lamprey to man (*97*). This points to the K2+3 supermodule as fulfilling a crucial role in determining the biological function of Pgn. The research reported here focuses on characterizing the structure and overall molecular dynamics of the K2 component of K2+3. The combined far-UV CD and NMR spectroscopic approach has proven to be most informative for a quantitative assessment of secondary and tertiary structural components. As we demonstrate, it is thanks to the CD evidence that significant 3_1-helix presence in the K2 domain was uncovered. This ought to be relevant both for the analysis of future kringle structures and, in general, for the visualization of novel protein foldings. The NMR solution structure of K2 suggests that the lower affinity of K2 for zwitterionic ligands is due to the shorter longitudinal axial dimension of the K2 LBS rather than to the presence of a basic residue at position 56 or of a Glu instead of an Asp residue at position 57. Combined with previously reported mutagenesis studies, our study reveals that functional differences among homologous domains can result from subtle structural factors that transmit through the global conformation since conservative amino acid residue replacements can effectively modulate the relative affinities for specific ligands in ways that cannot be directly predicted on the basis of standard assumptions for the local buildup of the binding site.

ACKNOWLEDGMENT

We are grateful to Klára Briknaróva for valuable assistance with the implementation of NMR pulse sequences and data processing routines and to Virgil Simplaceanu for expert help with the NMR spectrometers.

SUPPORTING INFORMATION AVAILABLE

A table containing NMR chemical shifts of plasminogen kringle 2 complexed to AMCHA (pH* 5.1 and 37 °C). This material is available free of charge via the Internet at http://pubs.acs.org.

REFERENCES

1. Lucas, M. A., Fretto, L. J., and McKee, P. A. (1983) *J. Biol. Chem. 258*, 4249−4256.
2. Wimann, B., Lijnen, H. R., and Collen, D. (1979) *Biochim. Biophys. Acta 579*, 142−154.
3. Lijnen, H. R., Hoylaerts, M., and Collen, D. (1980) *J. Biol. Chem. 255*, 10214−10222.
4. Silverstein, R. L., Leung, L. L. K., Harpel, P. C., and Nachman, R. L. (1984) *J. Clin. Invest. 74*, 1625−1633.
5. Ponting, C. P., Marshall, J. M., and Cederholm-Williams, S. A. (1992) *Blood Coagulation Fibrinolysis 3*, 605−614.
6. Miles, L. A., and Plow, E. F. (1985) *J. Biol. Chem. 260*, 4303−4311.
7. Hajjar, K. A., Harpel, P. C., Jaffe, E. A., and Nachman, R. L. (1986) *J. Biol. Chem. 261*, 11656−11662.
8. Cao, Y., Ji, R. W., Davidson, D., Schaller, J., Marti, D., Söhndel, S., McCance, S. G., O'Reilly, M. S., Llinás, M., and Folkman, J. (1996) *J. Biol. Chem. 271*, 29461−29467.
9. Cao, Y., Chen, A., An, S. S. A., Ji, R.-W., Davidson, D., Cao, Y., and Llinás, M. (1997) *J. Biol. Chem. 272*, 22924−22928.
10. Ji, W. R., Barrientos, L. G., Llinás, M., Gray, H., Villareal, X., DeFord, M. E., Castellino, F. J., Kramer, R. A., and Trail, P. A. (1998) *Biochem. Biophys. Res. Commun. 247*, 414−419.
11. Ji, W. R., Castellino, F. J., Chang, Y., DeFord, M. E., Gray, H., Villarreal, X., Kodri, M. E., Marti, D. N., Llinás, M., Schaller, J., Kramer, R. A., and Trail, P. A. (1998) *FASEB J. 15*, 1731−1738.
12. Llinás, M., De Marco, A., Hochschwender, S. M., and Laursen, R. A. (1983) *Eur. J. Biochem. 135*, 379−391.
13. Tulinsky, A., Park, C. H., and Skrypczak-Jankun, E. (1988) *J. Mol. Biol. 202*, 885−901.
14. Byeon, I.-J. L., and Llinás, M. (1991) *J. Mol. Biol. 222*, 1035−1051.
15. Wu, T.-P., Padmanabhan, K., Tulinsky, A., and Mulichak, A. M. (1991) *Biochemistry 30*, 10589−10594.
16. Rejante, M. R., and Llinás, M. (1994) *Eur. J. Biochem. 221*, 939−949.
17. Mathews, I. I., Vanderhoff-Hanaver, P., Castellino, F. J., and Tulinsky, A. (1996) *Biochemistry 35*, 2567−2576.
18. Mikol, V., LoGrasso, P. V., and Boettcher, B. R. (1996) *J. Mol. Biol. 256*, 751−761.
19. Motta, A., Laursen, R. A., Llinás, M., Tulinsky, A., and Park, C. H. (1987) *Biochemistry 26*, 3827−3836.
20. Thewes, T., Constantine, K., Byeon, I.-J. L., and Llinás, M. (1990) *J. Biol. Chem. 265*, 3906−3915.
21. Rejante, M. R., Byeon, I.-J. L., and Llinás, M. (1991) *Biochemistry 30*, 11081−11092.
22. Menhart, N., Sehl, L. C., Kelley, R. F., and Castellino, F. J. (1991) *Biochemistry 30*, 1948−1957.
23. Hoover, G. J., Menhart, N., Martin, A., Warder, S., and Castellino, F. J. (1993) *Biochemistry 32*, 10936−10943.
24. Nielsen, P. R., Einer-Jensen, K., Holtet, T. L., Andersen, B. D., Poulsen, F. M., and Thørgersen, H. C. (1993) *Biochemistry 32*, 13019−13025.
25. McCance, S. G., Menhart, N., and Castellino, F. J. (1994) *J. Biol. Chem. 269*, 32405−32410.
26. Marti, D., Schaller, J., Ochensberger, B., and Rickli, E. E. (1994) *Eur. J. Biochem. 219*, 455−462.
27. Söhndel, S., Hu, C.-K., Marti, D., Affolter, M., Schaller, J., Llinás, M., and Rickli, E. E. (1996) *Biochemistry 35*, 2357−2364.
28. An, S. S. A., Marti, D. N., Carreño, C., Albericio, F., Schaller, J., and Llinás, M. (1998) *Protein Sci. 7*, 1947−1959.
29. An, S. S. A., Carreño, C., Marti, D. N., Schaller, J., Albericio, F., and Llinás, M. (1998) *Protein Sci. 7*, 1960−1969.
30. Marti, D., Hu, C.-K., An, S. S. A., von Haller, P., Schaller, J., and Llinás, M. (1997) *Biochemistry 36*, 11591−11604.
31. Muchmore, D. C., McIntosh, L. P., Russell, C. B., Anderson, D. E., and Dahlquist, F. W. (1989) *Methods Enzymol. 177*, 44−73.
32. Johnson, W. C. (1999) *Proteins 35*, 307−312.
33. Aue, W. P., Bartholdi, E., and Ernst, R. R. (1976) *J. Chem. Phys. 64*, 2229−2246.
34. Piantini, U., Sørensen, O. W., and Ernst, R. R. (1982) *J. Am. Chem. Soc. 104*, 6800−6801.

35. Bax, A., and Davis, D. G. (1985) *J. Magn. Reson. 65*, 355−360.
36. Jeener, J., Meier, B. H., Bachmann, P., and Ernst, R. R. (1979) *J. Chem. Phys. 71*, 4546−4553.
37. Sklenar, V., Piotto, M., Leppik, R., and Saudek, V. (1993) *J. Magn. Reson., Ser. A 102*, 241−245.
38. Mori, S., Abeygunawardana, C., Johnson, M. O., and van Zijl, P. C. M. (1995) *J. Magn. Reson., Ser. B 108*, 94−98.
39. States, D. J., Haberkorn, R. A., and Ruben, D. J. (1982) *J. Magn. Reson. 48*, 286−292.
40. Zuiderweg, E. R. P., and Fesik, S. W. (1989) *Biochemistry 28*, 2387−2391.
41. Marion, D., Kay, L. E., Sparks, S. W., Torchia, D. A., and Bax, A. (1989) *J. Am. Chem. Soc. 111*, 1515−1517.
42. Marion, D., Driscoll, P. C., Kay, L. E., Wingfield, P. T., Bax, A., Gronenborn, A. M., and Clore, G. M. (1989) *Biochemistry 28*, 6150−6156.
43. Schleucher, J., Sattler, M., and Griesinger, C. (1993) *Angew. Chem., Int. Ed. 32*, 1489−1491.
44. Vuister, G. W., and Bax, A. (1993) *J. Am. Chem. Soc. 115*, 7772−7777.
45. Archer, S. J., Ikura, M., Torchia, D. A., and Bax, A. (1991) *J. Magn. Reson. 95*, 636−641.
46. Düx, P., Whitehead, B., Boelens, R., Kaptein, R., and Vuister, G. W. (1997) *J. Biomol. NMR 10*, 301−306.
47. Kay, L. E., Ikura, M., Tschudin, R., and Bax, A. (1990) *J. Magn. Reson. 89*, 496−414.
48. Grzesiek, S., and Bax, A. (1992) *J. Magn. Reson. 96*, 432−440.
49. Bax, A., and Ikura, M. (1991) *J. Biomol. NMR 1*, 99−104.
50. Montelione, G. T., Lyons, B. A., Emerson, S. D., and Tashiro, M. (1992) *J. Am. Chem. Soc. 114*, 10974−10975.
51. Grzesiek, S., Anglister, J., and Bax, A. (1993) *J. Magn. Reson., Ser. B 101*, 114−119.
52. Carlomagno, T., Maurer, M., Sattler, M., Schwendinger, M. G., Glaser, S. J., and Griesinger, C. (1996) *J. Biomol. NMR 8*, 161−170.
53. Shaka, A. J., Lee, C. J., and Pines, A. (1988) *J. Magn. Reson. 77*, 274−293.
54. Shaka, A. J., Keeler, J., Frenkiel, T., and Freeman, R. (1983) *J. Magn. Reson. 52*, 335−338.
55. De Marco, A. (1977) *J. Magn. Reson. 26*, 527−528.
56. Live, D. H., Davis, D. G., Agosta, W. C., and Cowburn, D. (1984) *J. Am. Chem. Soc. 106*, 1939−1943.
57. De Marco, A., Llinás, M., and Wüthrich, K. (1978) *Biopolymers 17*, 617−636.
58. Pardi, A., Billeter, M., and Wüthrich, K. (1984) *J. Mol. Biol. 180*, 741−751.
59. Brünger, A. T. (1992) *X-PLOR 3.1 User Manual*, Yale University Press, New Haven, CT.
60. Nilges, M., Kuszewsky, J., and Brünger, A. T. (1991) in *Computational Aspects of the Study of Biological Macromolecules by NMR* (Hoch, J. C., Ed.) Plenum Press, New York.
61. Kuszewsky, J., Nilges, M., and Brünger, A. T. (1992) *J. Biomol. NMR 2*, 33−56.
62. Laskowsky, R. A., MacArthur, M. W., Moss, D. S., and Thornton, J. M. (1993) *J. Appl. Crystallogr. 26*, 283−291.
63. Koradi, R., Billeter, M., and Wüthrich, K. (1996) *J. Mol. Graphics 14*, 51−55.
64. King, S. M., and Johnson, W. C. (1999) *Proteins 35*, 307−312.
65. Dayie, K. T., and Wagner, G. (1994) *J. Magn. Reson., Ser. A 111*, 121−126.
66. Lipari, G., and Szabo, A. (1982) *J. Am. Chem. Soc. 104*, 4546−4559.
67. Lipari, G., and Szabo, A. (1982) *J. Am. Chem. Soc. 104*, 4559−4570.
68. Palmer, A. G., Rance, M., and Wright, P. E. (1991) *J. Am. Chem. Soc. 113*, 4371−4380.
69. Venyaminov, S. Y., and Yang, J. T. (1996) in *Circular dichroism and the conformational analysis of biomolecules* (Fasman, G. D., Ed.) pp 69−107, Plenum Press, New York.
70. De Marco, A., Pluck, N. D., Bányai, L., Trexler, M., Laursen, R. A., Patthy, L., Llinás, M., and Williams, R. J. P. (1985) *Biochemistry 24*, 748−753.
71. Li, X., Bokman, A. M., Llinás, M., Smith, R. A. G., and Dobson, C. M. (1994) *J. Mol. Biol. 235*, 1548−1559.
72. Chang, Y., Mochalkin, I., McCance, S. G., Cheng, B., Tulinsky, A., and Castellino, F. J. (1998) *Biochemistry 37*, 3258−3271.
73. Wishart, D. S., Skyes, B. D., and Richards, F. M. (1991) *J. Mol. Biol. 222*, 311−333.
74. Adzhubei, A. A., and Sternberg, M. J. E. (1993) *J. Mol. Biol. 229*, 472−493.
75. Sreerama, N., and Woody, R. W. (1994) *Biochemistry 33*, 10022−10025.
76. Wüthrich, K. (1986) *NMR of proteins and nucleic acids*, John Wiley and Sons, New York.
77. Mulichak, A. M., Tulinsky, A., and Ravichandran, K. G. (1991) *Biochemistry 30*, 10576−10588.
78. de Vos, A. M., Ultsch, M. H., Kelley, R. F., Padmanabhan, K., Tulinsky, A., Westbrook, M. L., and Kossiakoff, A. A. (1992) *Biochemistry 31*, 270−279.
79. Ramesh, V., Gyenes, M., Patthy, L., and Llinás, M. (1986) *Eur. J. Biochem. 159*, 581−595.
80. Roseman, M. A. (1988) *J. Mol. Biol. 200*, 513−522.
81. Tulinsky, A., Park, C. H., Mao, B., and Llinás M. (1988) *Proteins: Struct., Funct., Genet. 3*, 85−96.
82. Trexler, M., Váli, Z., and Patthy, L. (1982) *J. Biol. Chem. 257*, 7401−7406.
83. Chang, Y., Zajicek, J., and Castellino, F. J. (1997) *Biochemistry 36*, 7652−7663.
84. Rejante, M. R. (1992) Ph.D. Dissertation, Carnegie Mellon University, Pittsburgh, PA.
85. De Marco, A., Petros, A. M., Laursen, R. A., and Llinás, M. (1987) *Eur. Biophys. J. 14*, 359−368.
86. Byeon, I.-J. L., Kelley, R. F., Mulkerrin, M. G., An, S. S. A., and Llinás, M. (1995) *Biochemistry 34*, 2739−2750.
87. Cox, M., Schaller, J., Boelens, R., Kaptein, R., Rickli, E., and Llinás, M. (1994) *Chem. Phys. Lipids 67/68*, 43−58.
88. Ramesh, V., Petros, A. M., Llinás, M., Tulinsky, A., and Park, C. H. (1987) *J. Mol. Biol. 198*, 481−498.
89. King, S. M., and Johnson, W. C. (1999) *Proteins 35*, 313−320.
90. Castellino, F. J., de Serrano, V. S., Powell, J. R., Johnson, W. R., and Beals, J. M. (1986) *Arch. Biochem. Biophys. 247*, 312−320.
91. Cleary, S., Mulkerrin, M. G., and Kelley, R. F. (1989) *Biochemistry 28*, 1884−1891.
92. Wu, T.-P., Padmanabhan, K., and Tulinsky, A. (1994) *Blood Coagulation Fibrinolysis 5*, 157−166.
93. Mochalkin, I., Cheng, B., Klezovitch, O., Scanu, A. M., and Tulinsky, A. (1999) *Biochemistry 38*, 1990−1998.
94. Ultsch, M., Lokker, N. A., Godowski, P. J., and de Vos, A. M. (1998) *Structure 6*, 1383−1393.
95. Seshadri, T. P., Tulinsky, A., Skrzypczak-Jankun, E., and Park, C. H. (1991) *J. Mol. Biol. 220*, 481−494.
96. Arni, R. K., Padmanabhan, K., Padmanabhan, K. P., Wu, T.-P., and Tulinsky, A. (1993) *Biochemistry 32*, 4727−4737.
97. Affolter, M., Schaller, J., and Rickli, E. E. (1993) *Protein Sequences Data Anal. 5*, 207−211.

BI9917378